Supporting Information

A Cooperative Adsorbent for the Switch-Like Capture of Carbon Dioxide from Crude Natural Gas

Rebecca L. Siegelman,[ab] Joshua A. Thompson,[cd] Jarad A. Mason,[ae] Thomas M. McDonald,[a] and Jeffrey R. Long*[abf]

[a]*Department of Chemistry, University of California, Berkeley, CA 94720, USA*
[b]*Materials Sciences Division, Lawrence Berkeley National Laboratory, Berkeley, CA 94720, USA*
[c]*Chevron Energy Technology Company, Richmond, CA 94801, USA*
[d]*Current address: Oak Ridge National Laboratory, Oak Ridge, TN 37830, USA*
[e]*Current address: Harvard University, Cambridge, MA 02138, USA*
[f]*Department of Chemical and Biomolecular Engineering, University of California, Berkeley, CA 94720, USA*

*Correspondence to jrlong@berkeley.edu

Table of Contents

1. Characterization of Mg_2(dobpdc)

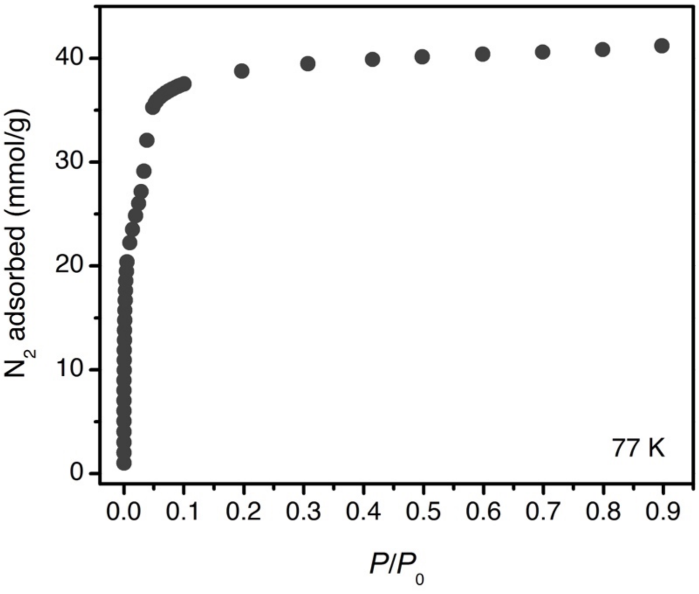

Figure S1. Surface area measurement of Mg_2(dobpdc) with N_2 at 77 K. The Brunauer-Emmett-Teller (BET) surface area was calculated as 2520 ± 40 m^2/g, and the Langmuir surface area was calculated as 4090 ± 12 m^2/g.

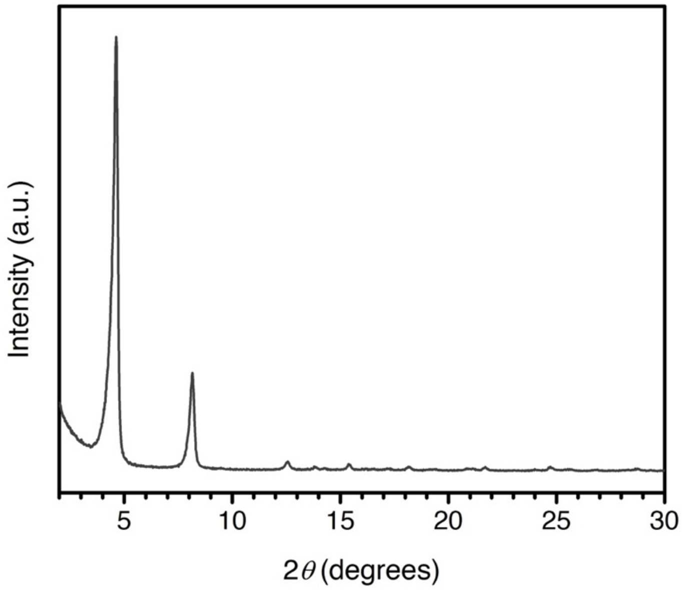

Figure S2. Laboratory powder X-ray diffraction pattern (λ = 1.5418 Å) of activated Mg_2(dobpdc) in air.

2. Additional Characterization of ii-2–Mg_2(dobpdc)

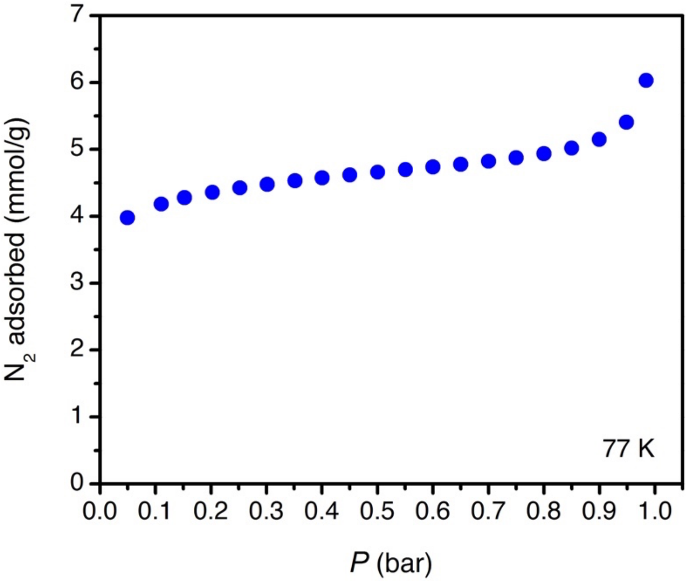

Figure S3. Surface area measurement of ii-2–Mg_2(dobpdc) with N_2 at 77 K. The Langmuir surface area was calculated as 490 ± 4 m^2/g. A pore volume of 0.17 cm^3/g was calculated from the loading at $P/P_0 = 0.70$.

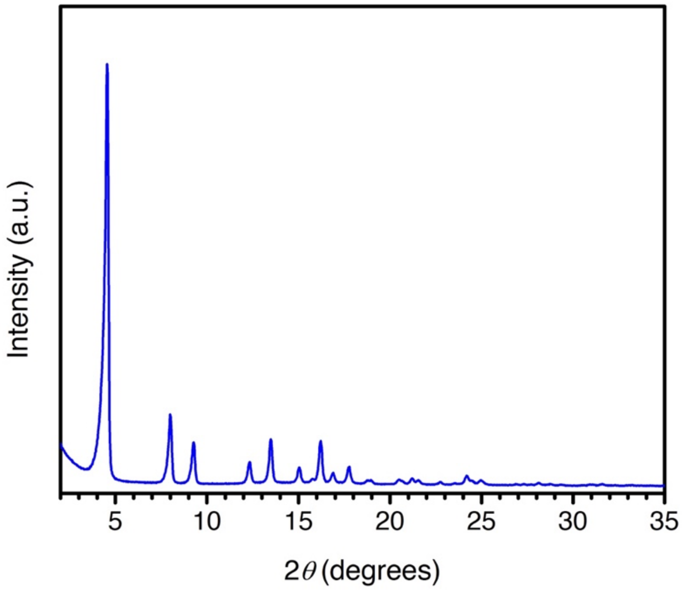

Figure S4. Laboratory powder X-ray diffraction pattern (λ = 1.5418 Å) for as-synthesized ii-2–Mg_2(dobpdc).

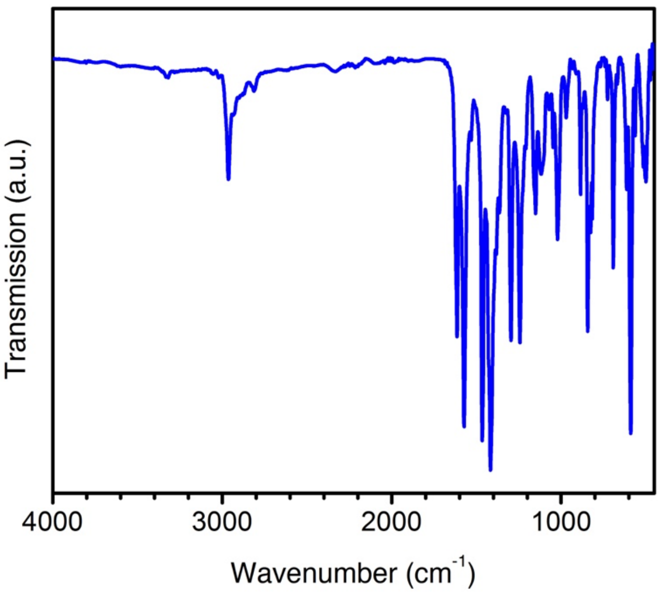

Figure S5. Infrared spectrum of ii-2–Mg_2(dobpdc) following activation from hexanes.

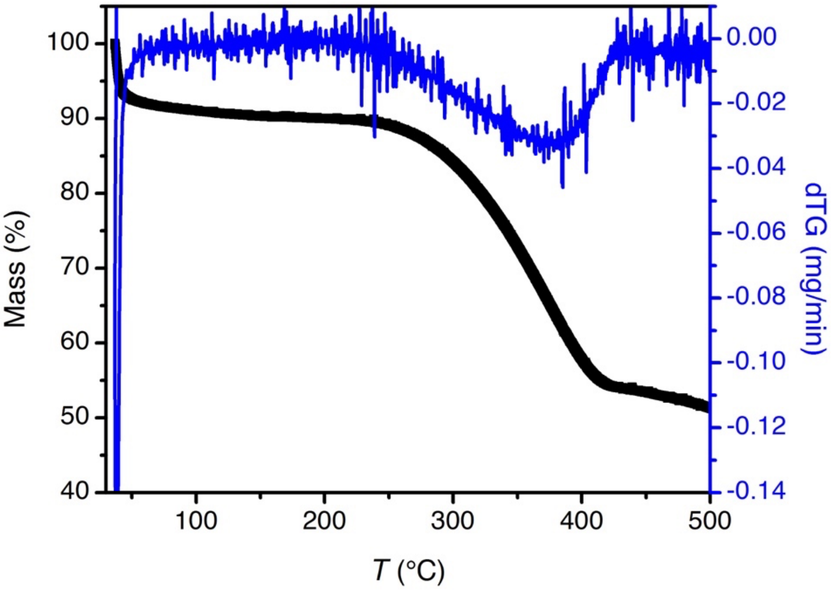

Figure S6. Thermogravimetric decomposition traces (black) and derivative decomposition traces (dTG, blue) for ii-2–Mg_2(dobpdc). A temperature ramp rate of 2 °C/min was used. The dTG peak at lowest temperature is due to excess solvent (toluene or hexanes) in the framework pores, while the higher temperature peak is due to volatilization of the diamine.

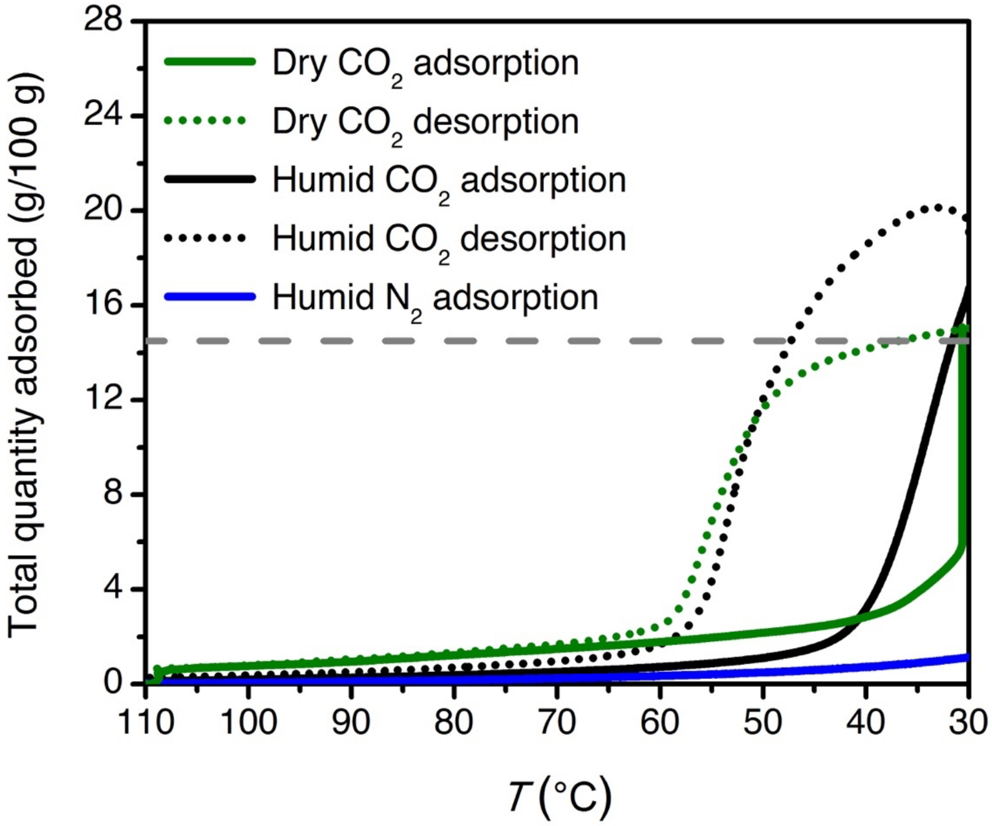

Figure S7. Dry (green) and humid (black) adsorption (solid lines) and desorption (dotted lines) isobars for pure CO_2, as well as a humid N_2 adsorption isobar (blue), for ii-2–Mg_2(dobpdc). The material was activated at 110 °C under flowing dry (green) or humid (black) N_2 for 20 min. A ramp rate of 1 °C/min was used, and isobars were collected at atmospheric pressure. The expected adsorption capacity corresponding to 1 CO_2 per diamine is indicated as a dashed gray line. For the dry CO_2 isobar, the temperature was held isothermally at 30 °C for 45 min prior to beginning the desorption branch of the isobar. The dry CO_2 isobar is reproduced from reference 1.

3. Additional Characterization of ee-2–Mg_2(dobpdc)

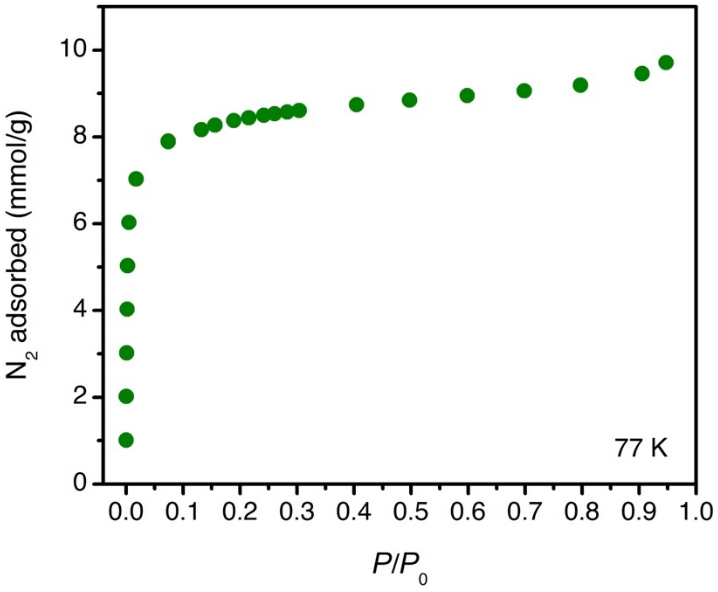

Figure S8. Surface area measurement of ee-2–Mg_2(dobpdc) with N_2 at 77 K. The Brunauer-Emmett-Teller (BET) surface area was calculated as 726 ± 2 m^2/g, and the Langmuir surface area was calculated as 911 ± 4 m^2/g. A pore volume of 0.32 cm^3/g was calculated from the loading at $P/P_0 = 0.80$.

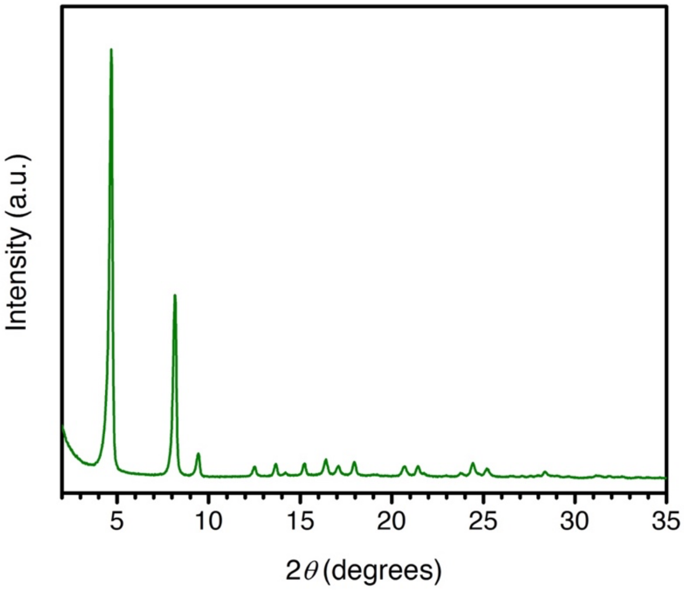

Figure S9. Laboratory powder X-ray diffraction pattern (λ = 1.5418 Å) for as-synthesized ee-2–Mg_2(dobpdc).

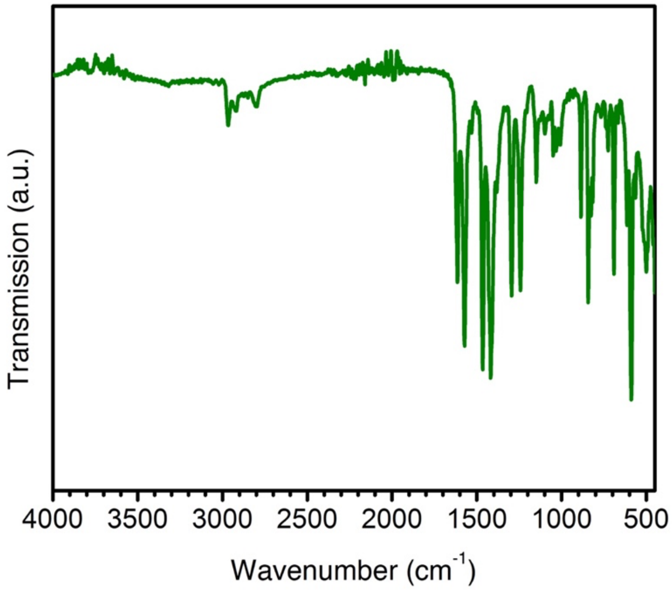

Figure S10. Infrared spectrum of ee-2–Mg_2(dobpdc) following activation from hexanes.

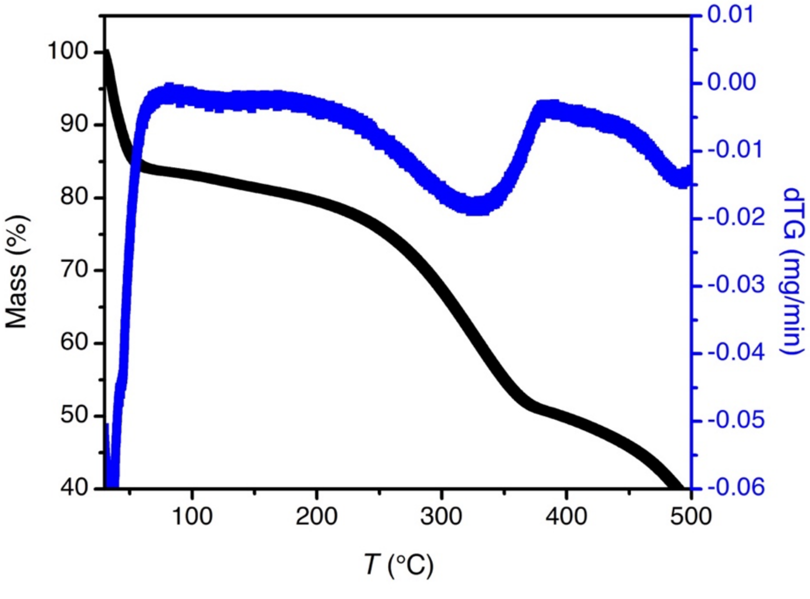

Figure S11. Thermogravimetric decomposition traces (black) and derivative decomposition traces (dTG, blue) for ee-2–Mg_2(dobpdc). A temperature ramp rate of 2 °C/min was used. The dTG peak at lowest temperature is due to excess solvent (toluene or hexanes) in the framework pores, while the higher temperature peak is due to volatilization of the diamine.

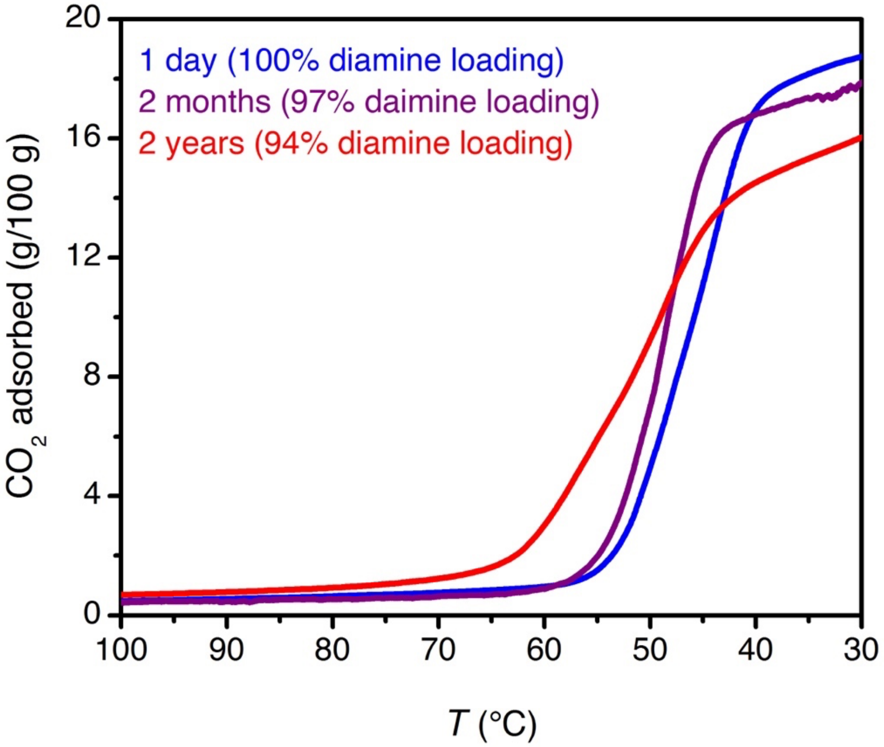

Figure S12. Pure CO_2 adsorption isobars of ee-2–Mg_2(dobpdc) after storage in a sealed vial in air for 1 day (blue), 2 months (purple), and 2 years (red). The reported diamine loadings were determined after isobar collection by digesting the samples with DCl following the procedure in the main text and comparing the diamine and ligand peak integrals in the NMR spectra.

4. Isotherm Backgrounds and Fits

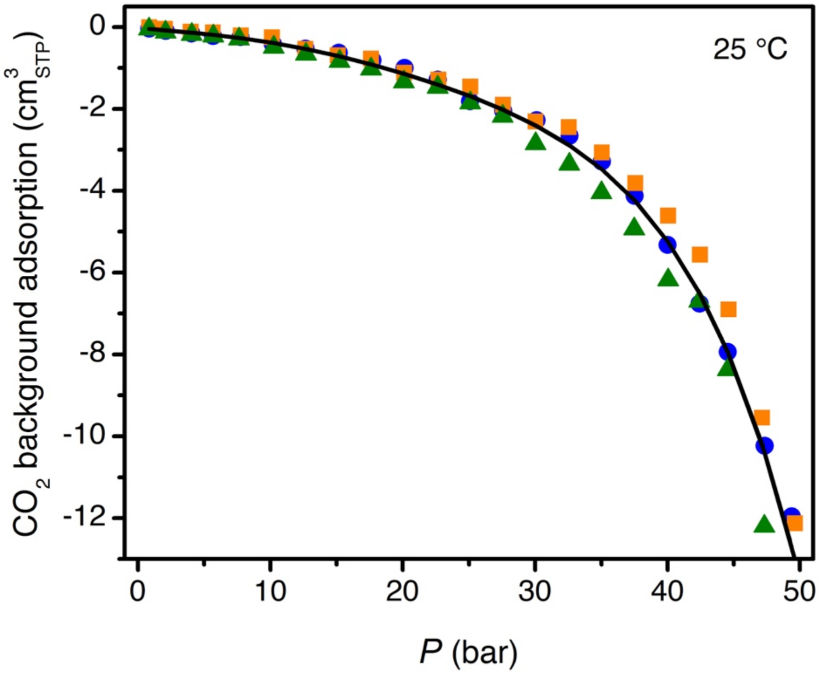

Figure S13. Three background CO$_2$ adsorption isotherms (symbols) at 25 °C for an empty high-pressure sample holder. The black line represents a 5th order polynomial fit to the background adsorption and was used to correct high-pressure adsorption data at 25 °C. The same background correction procedure was used for high-pressure data at other temperatures. The negative background adsorption likely results from a temperature gradient between the exposed portion of the sample holder and the portion in the isothermal bath.

Type I isotherms for each material were fit with a single- or dual-site Langmuir ($v_i = 1$) or Langmuir–Freundlich ($v_i \neq 1$) equation (eqn S1), where q is the total amount adsorbed in mmol/g, P is the pressure in bar, $q_{\mathrm{sat},i}$ is the saturation capacity in mmol/g, and b_i is the Langmuir parameter in bar^{-v} for up to two sites 1 and 2. Isotherms were fit either individually at each temperature or simultaneously as a function of temperature, as specified in the figure and table captions. For simultaneous fits, the Langmuir parameter was expressed using eqn S2, where S_i is the site-specific molar entropy of adsorption in J/mol·K, E_i is the site-specific binding energy in kJ/mol, R is the gas constant in J/mol·K, and T is the temperature in K. The fit parameters for each material can be found alongside the corresponding fits in Sections S5–7 below.

$$q = \frac{q_{sat,1} b_1 P^{v_1}}{1+b_1 P^{v_1}} + \frac{q_{sat,2} b_2 P^{v_2}}{1+b_2 P^{v_2}} \qquad \text{(S1)}$$

$$b_i = e^{-\frac{S_i}{R}} e^{E_i \cdot \frac{1000}{RT}} \qquad \text{(S2)}$$

5. Additional Isotherms, Fits, and Thermodynamic Data for ii-2–Mg_2(dobpdc)

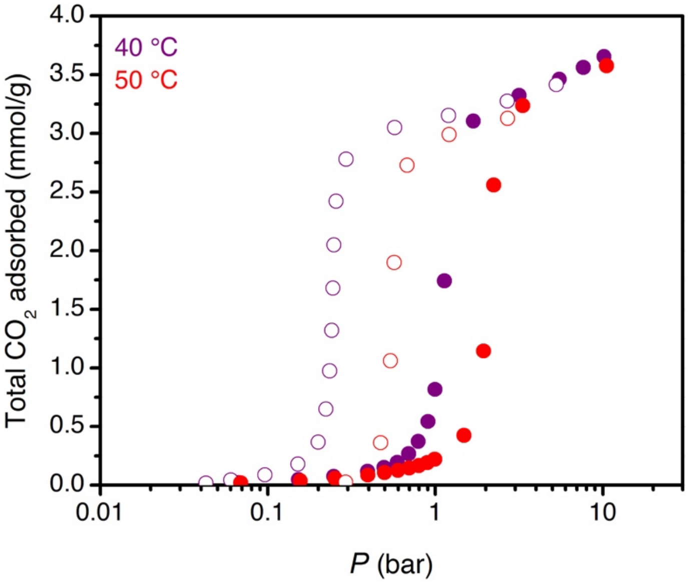

Figure S14. High-pressure CO_2 adsorption (filled circles) and desorption (open circles) isotherms for ii-2–Mg_2(dobpdc). A maximum of 60 min was allotted for equilibration for each data point.

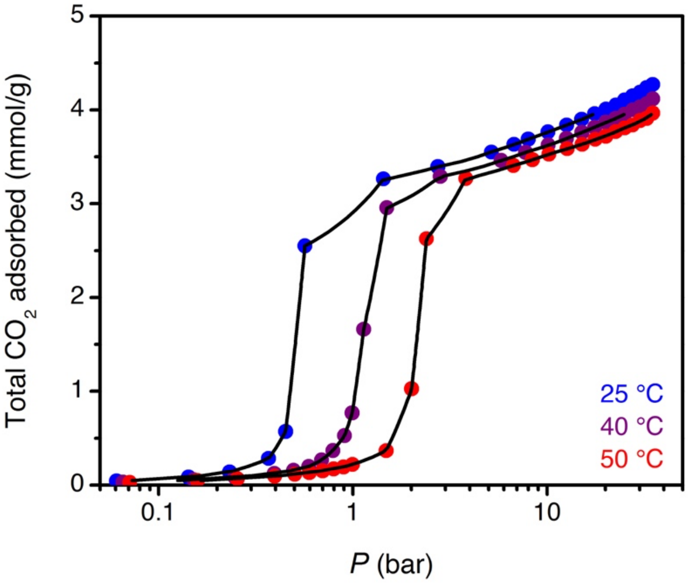

Figure S15. Spline interpolation of CO_2 isotherms for ii-2–Mg_2(dobpdc) used in the calculation of loading-dependent differential enthalpies and entropies of adsorption.

Using the adsorption enthalpy of −45 kJ/mol CO_2 within the cooperative adsorption step and the measured step onset pressure of 1 bar at 40 °C, the step onset pressure can be predicted at any temperature using the Clausius–Clapeyron relationship, as shown in eqn S3:

$$p_{step}(T) = p_{step,T_0} e^{\left(\frac{\Delta H_{step}}{R}\right)\left(\frac{1}{T_0}-\frac{1}{T}\right)} \tag{S3}$$

Here, $p_{step,T0}$ is a reference step pressure at temperature T_0 in (K), ΔH_{step} is the differential adsorption enthalpy in kJ/mol within the cooperative adsorption step, and R is the universal gas constant in kJ/(mol·K).

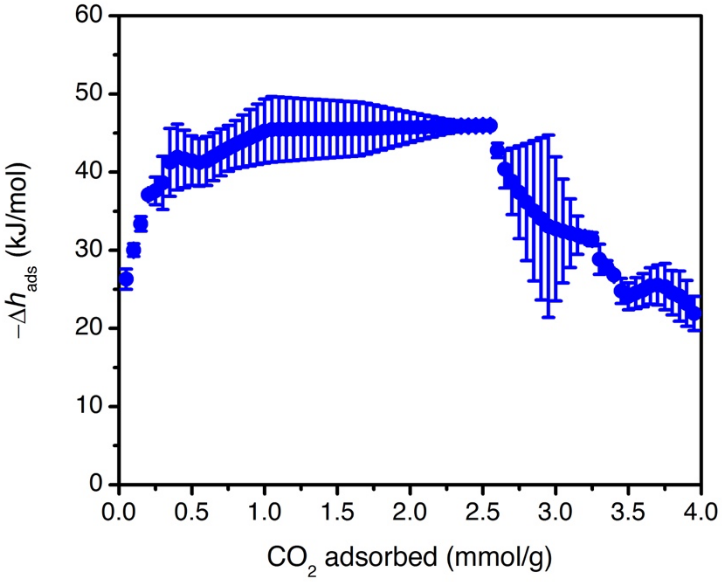

Figure S16. Loading-dependent differential enthalpy of CO_2 adsorption for ii-2–Mg_2(dobpdc) calculated from spline interpolation of the CO_2 adsorption isotherms at 25, 40, and 50 °C.

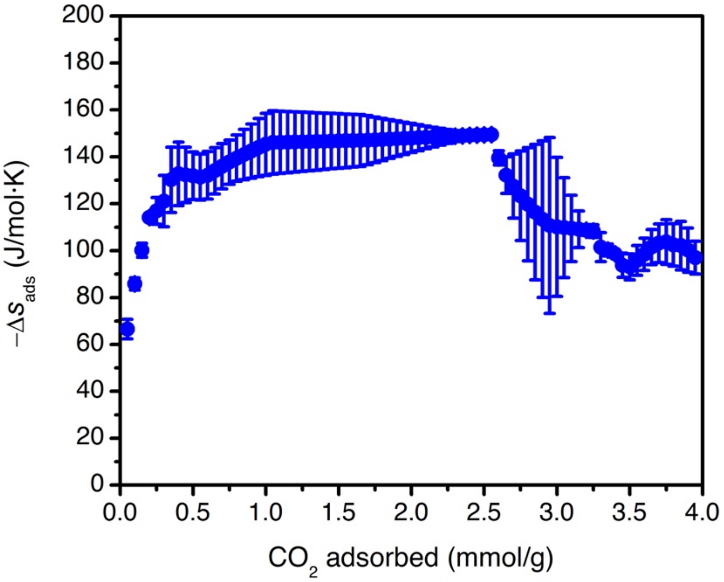

Figure S17. Loading-dependent differential entropy of CO_2 adsorption for ii-2–Mg_2(dobpdc) calculated from spline interpolation of the CO_2 adsorption isotherms at 25, 40, and 50 °C.

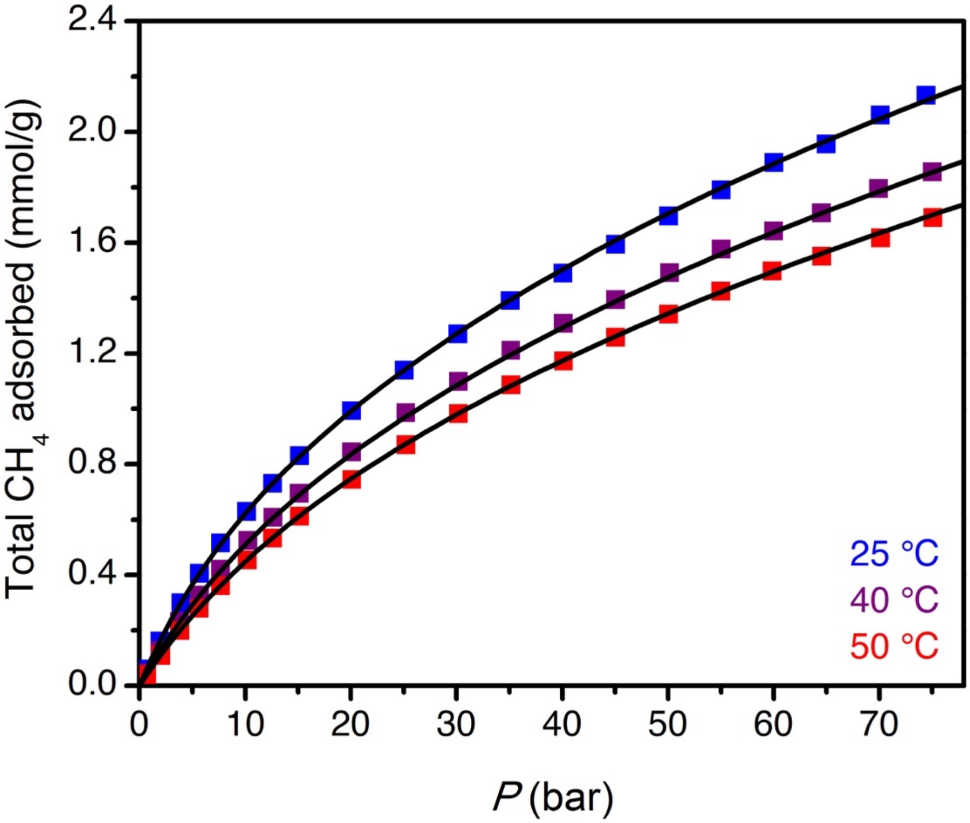

Figure S18. High-pressure CH_4 adsorption isotherms for ii-2–Mg_2(dobpdc) (squares) and corresponding simultaneous dual-site Langmuir fits (black lines).

Table S1. Dual-site Langmuir fit parameters for the CH_4 adsorption isotherms of ii-2–Mg_2(dobpdc) at 25, 40, and 50 °C (fit simultaneously for all temperatures); $q_{sat,i}$ is the saturation capacity, Si is the site-specific molar entropy of adsorption, E_i is the site-specific binding energy, and R is the gas constant in J/mol·K.

$q_{sat,1}$ (mmol/g)	$-S_1$ (R)	$-E_1$ (kJ/mol)	$q_{sat,2}$ (mmol/g)	$-S_2$ (R)	$-E_2$ (kJ/mol)
0.88	8.6	15.2	5	10.5	12.8

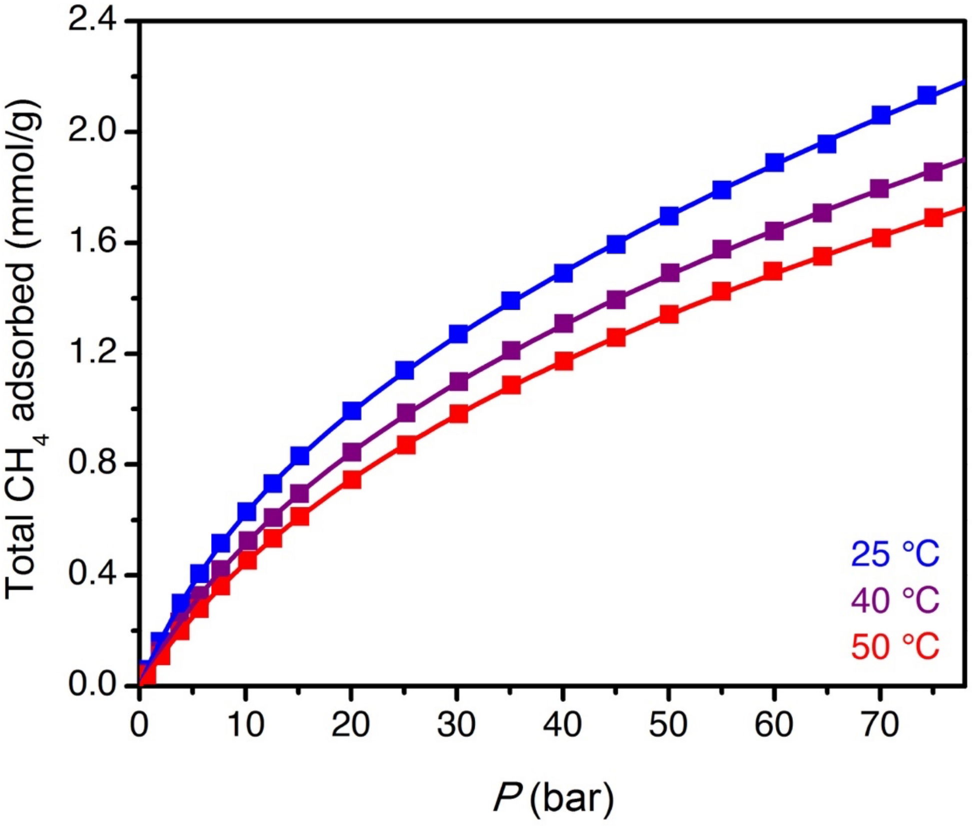

Figure S19. High-pressure CH_4 adsorption isotherms for ii-2–Mg_2(dobpdc) (squares) and corresponding dual-site Langmuir fits at individual temperatures (lines).

Table S2. Dual-site Langmuir fit parameters for the CH_4 adsorption isotherms of ii-2–Mg_2(dobpdc) at 25, 40, and 50 °C (fit independently for all temperatures); $q_{sat,i}$ is the saturation capacity, S_i is the site-specific molar entropy of adsorption, E_i is the site-specific binding energy, and R is the gas constant in J/mol·K.

T (K)	$q_{sat,1}$ (mmol/g)	$-S_1$ (R)	$-E_1$ (kJ/mol)	$q_{sat,2}$ (mmol/g)	$-S_2$ (R)	$-E_2$ (kJ/mol)
298	1.1	8.0	13.2	8.0	7.2	3.0
313	1.0	8.0	13.1	5.3	7.1	3.6
323	1.0	6.9	10.0	4.7	6.8	3.0

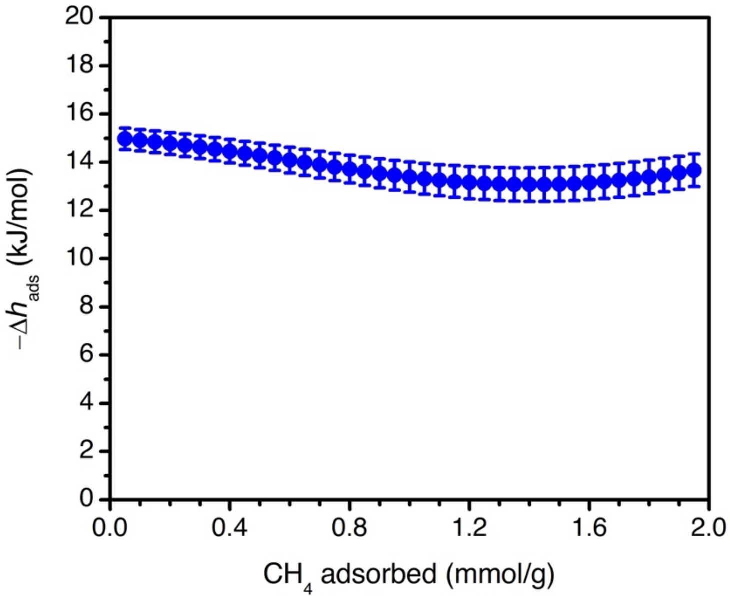

Figure S20. Loading-dependent differential enthalpy of CH_4 adsorption for ii-2–Mg_2(dobpdc), as calculated from individual, dual-site Langmuir fits of the high-pressure total adsorption isotherms at 25, 40, and 50 °C.

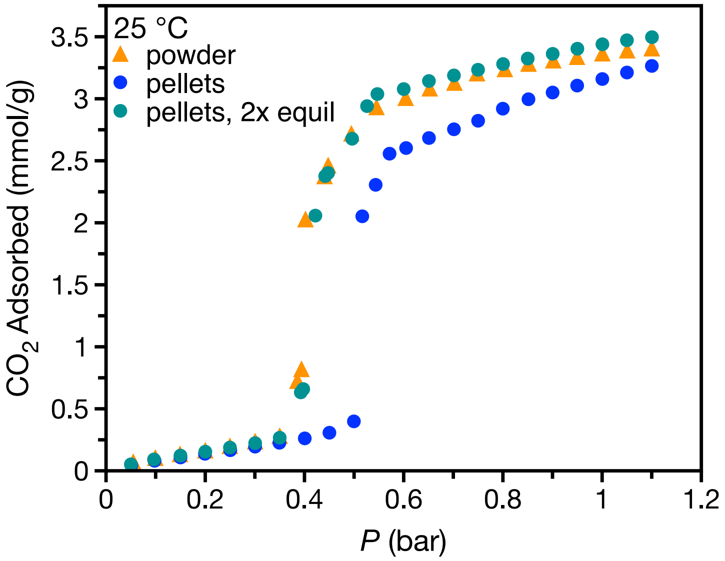

Figure S21. Comparison of low-pressure CO_2 adsorption isotherms at 25 °C for as-synthesized ii-2–Mg_2(dobpdc) powder (orange triangles), 25–45 mesh binderless pellets (blue circles), and the pelletized adsorbent with twice the standard equilibration time (teal circles). Equilibration is defined as <0.01% change in pressure over an average of 11 intervals of the user-specified equilibration interval, with the standard interval set as 15 s. The isotherm of the pelletized adsorbent was found to match that of the powder only when longer equilibration times were allotted, consistent with a kinetics limitation.

6. Additional Isotherms, Fits, and Thermodynamic Data for ee-2–Mg_2(dobpdc)

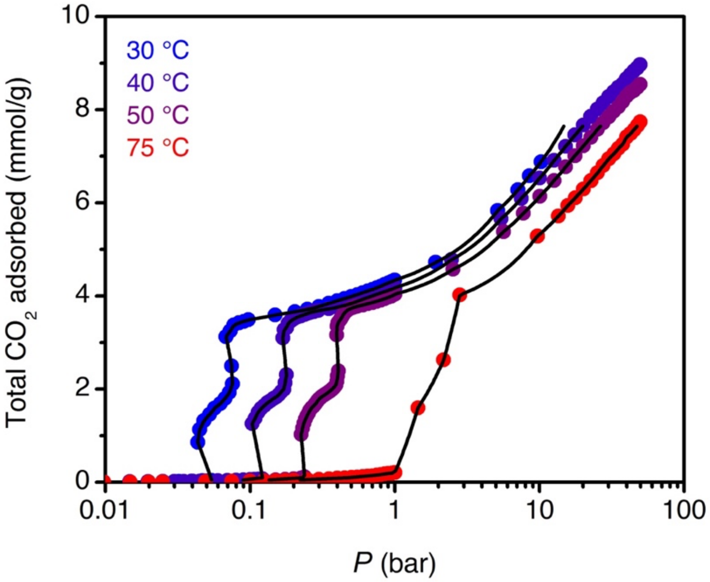

Figure S22. Spline interpolation of CO_2 isotherms (black lines) for ee-2–Mg_2(dobpdc) used in the calculation of loading-dependent differential enthalpies and entropies of adsorption.

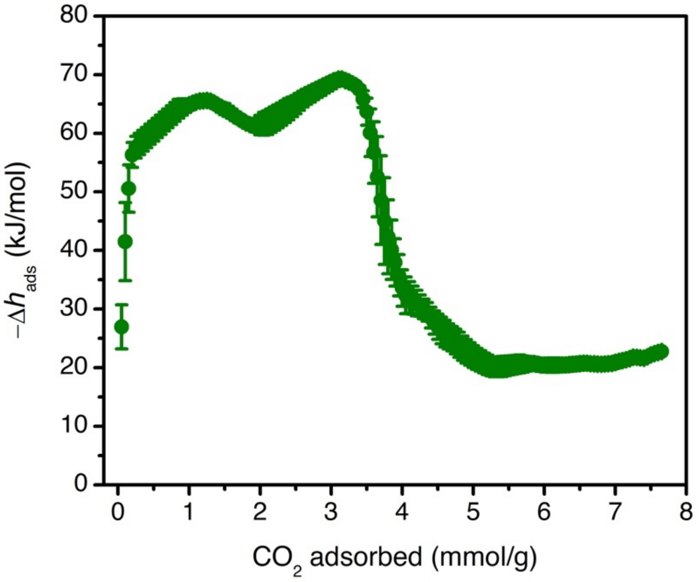

Figure S23. Loading-dependent differential enthalpy of CO_2 adsorption for ee-2–Mg_2(dobpdc) calculated from spline interpolation of the CO_2 adsorption isotherms at 30, 40, 50, and 75 °C.

Using the average adsorption enthalpy of −64 kJ/mol CO_2 within the first cooperative adsorption step and the measured onset pressure of 0.24 bar for the first adsorption step at 50 °C, the step onset pressure for the first step can be predicted at any temperature using the Clausius–Clapeyron relationship, as shown in Equation S3.

Table S3. Measured onset pressures for the first cooperative CO_2 adsorption step of ee-2–Mg_2(dobpdc), and onset pressures predicted from the Clausius–Clapeyron relationship and a reference step pressure of 0.24 bar at 50 °C.

T (°C)	$P_{\text{step, measured}}$ (bar)	$P_{\text{step, predicted}}$ (bar)
25	0.02	0.03
30	0.05	0.05
40	0.11	0.11
55	not measured	0.35
60	not measured	0.50
65	not measured	0.70
70	not measured	0.98
75	$1.0 < P_{\text{step}} < 1.4$	1.36

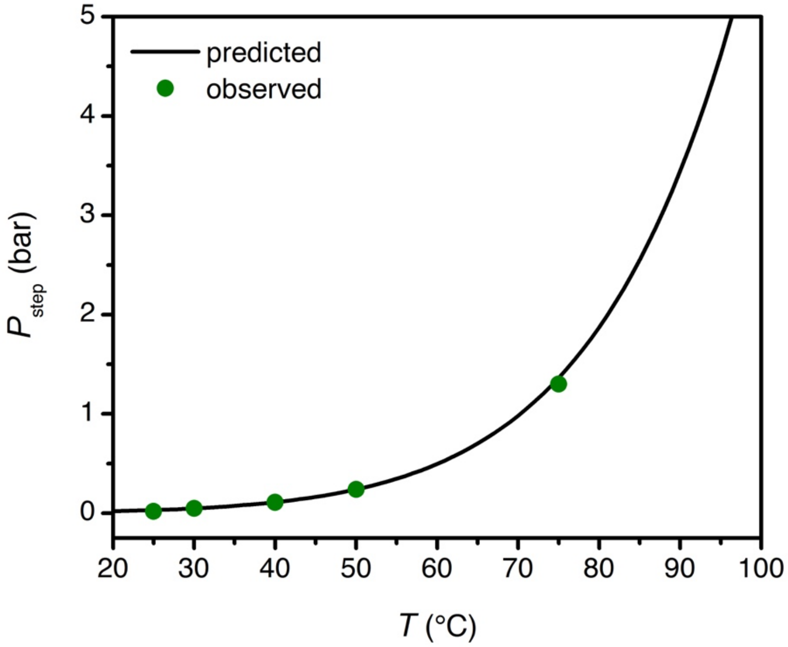

Figure S24. Measured onset pressures for the first cooperative CO_2 adsorption step of ee-2–Mg_2(dobpdc), and onset pressures predicted from the Clausius–Clapeyron relationship.

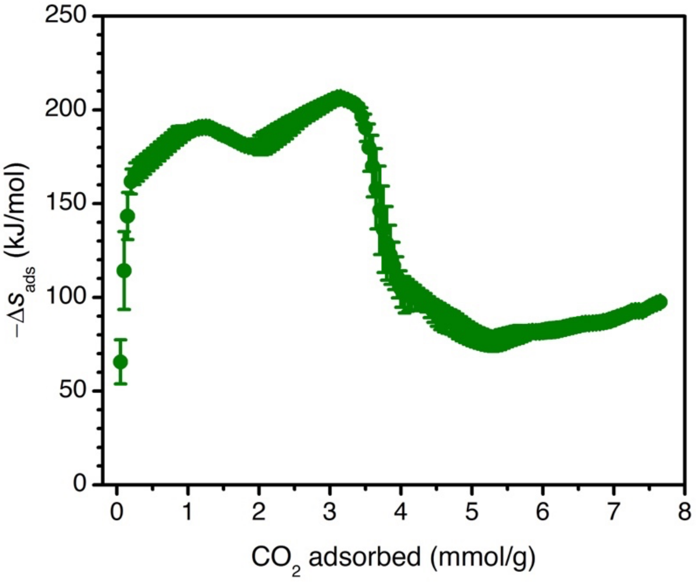

Figure S25. Loading-dependent differential entropy of CO_2 adsorption for ee-2–Mg_2(dobpdc) calculated from spline interpolation of the CO_2 adsorption isotherms at 30, 40, 50, and 75 °C.

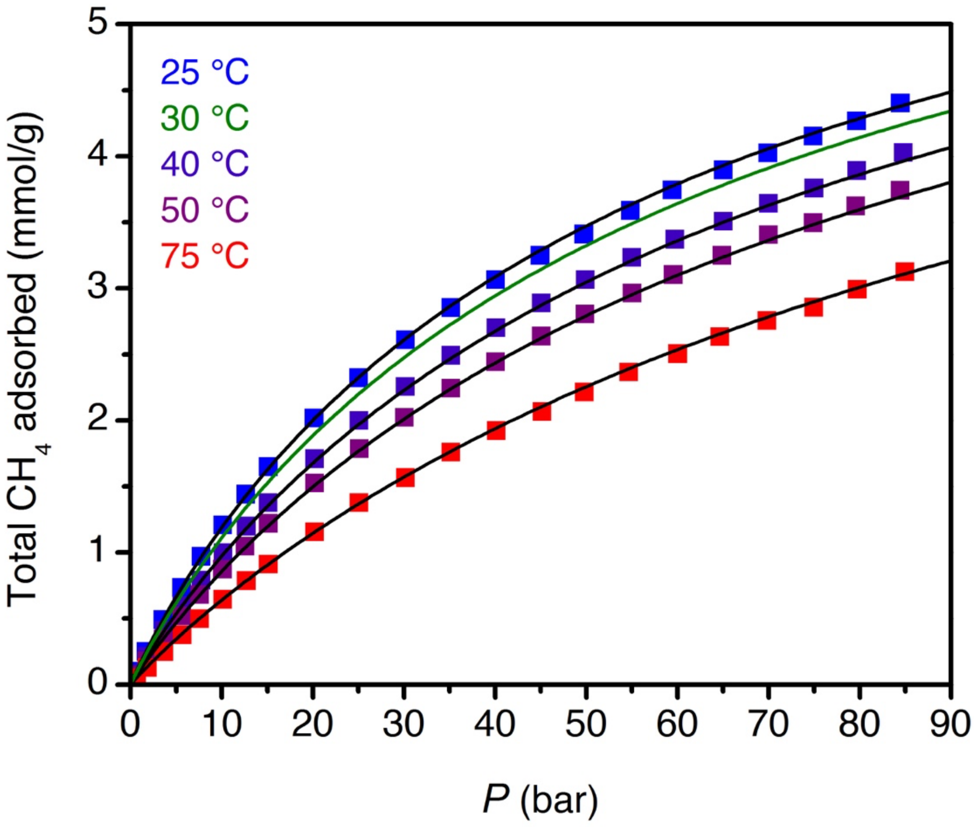

Figure S26. High-pressure CH_4 adsorption isotherms for ee-2–Mg_2(dobpdc) (squares) and corresponding simultaneous single-site Langmuir fits (black lines). The green line shows the simulated CH_4 adsorption isotherm at 30 °C, the temperature used for several breakthrough experiments in this work.

Table S4. Single-site Langmuir fit parameters for the CH_4 adsorption isotherms of ee-2–Mg_2(dobpdc) at 25, 40, 50, and 75 °C (fit simultaneously for all temperatures); q_{sat} is the saturation capacity, S is the site-specific molar entropy of adsorption, E is the site-specific binding energy, and R is the gas constant in J/mol·K.

q_{sat} (mmol/g)	$-S$ (R)	$-E$ (kJ/mol)
7.33	8.75	12.2

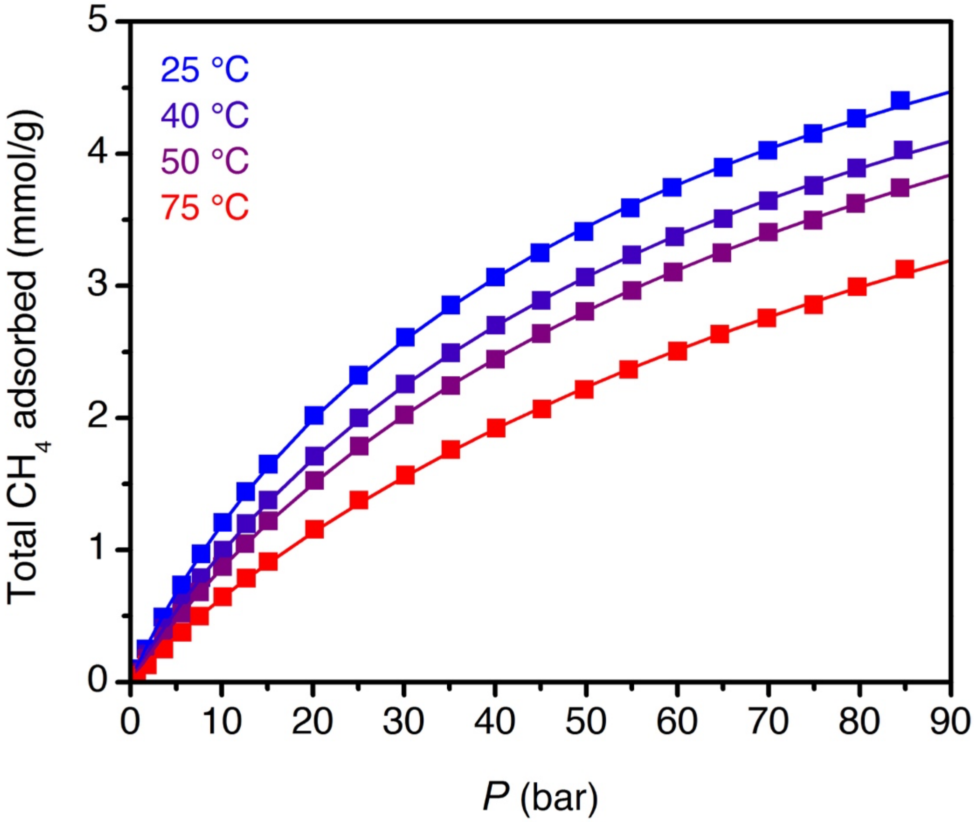

Figure S27. High-pressure CH_4 adsorption isotherms for ee-2–Mg_2(dobpdc) (squares) and corresponding single-site Langmuir–Freundlich fits at individual temperatures (lines).

Table S5. Single-site Langmuir–Freundlich fit parameters for the CH_4 adsorption isotherms of ee-2–Mg_2(dobpdc) at 25, 40, 50, and 75 °C (fit independently for all temperatures); q_{sat} is the saturation capacity, *b* is the Langmuir constant, and *v* is the Freundlich parameter.

T **(K)**	q_{sat} **(mmol/g)**	***b*** **(bar^{-v})**	***v***
298	7.54	0.0220	0.932
313	7.37	0.0170	0.955
323	7.561	0.0145	0.948
348	7.684	0.0104	0.939

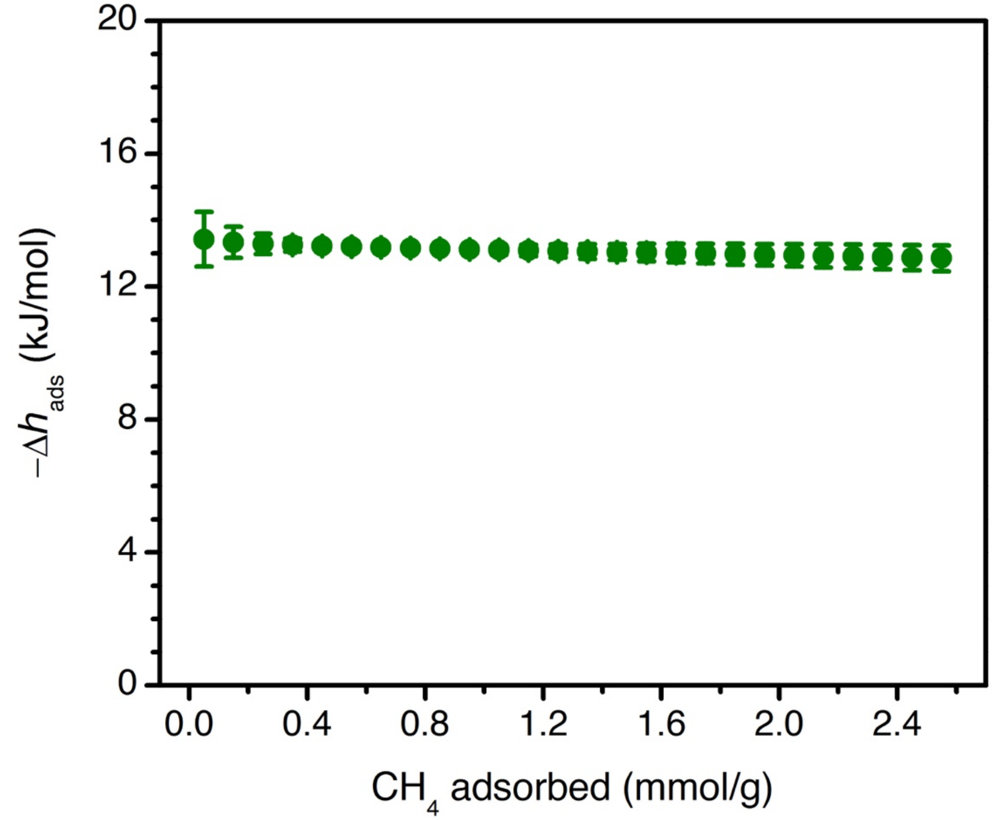

Figure S28. Loading-dependent differential enthalpy of CH_4 adsorption for ee-2–Mg_2(dobpdc), as calculated from individual, single-site Langmuir–Freundlich fits of the high-pressure total adsorption isotherms at 25, 40, 50, and 75 °C.

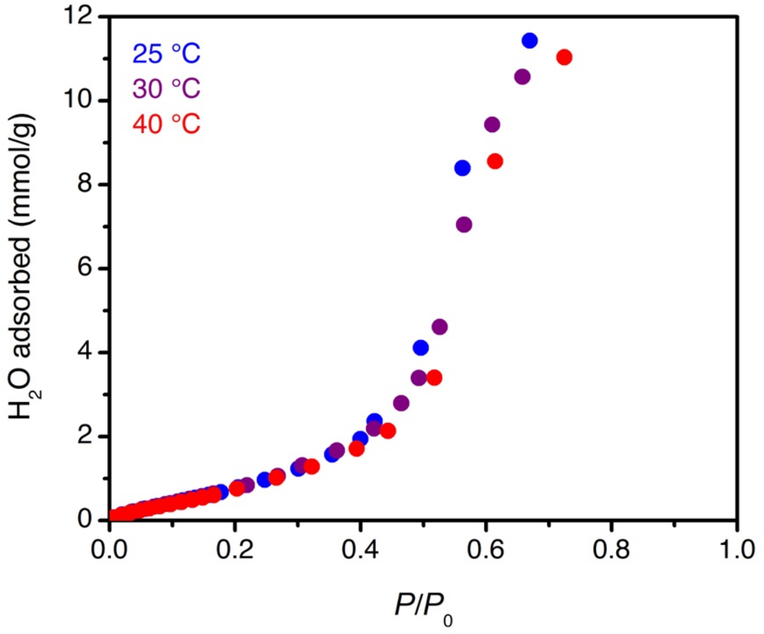

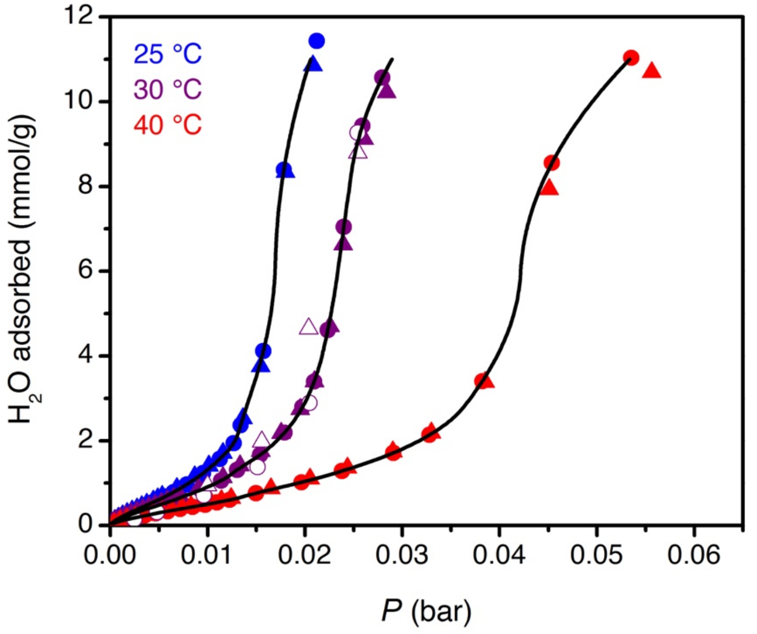

Figure S29. Adsorption (filled symbols) and desorption (open symbols) H_2O isotherms for ee-2–Mg_2(dobpdc) powder (circles) and pellets (triangles). Data are plotted as a function of both relative pressure (top) and absolute pressure (bottom). The black lines in the absolute pressure plot depict the second-order spline interpolation used to calculate the loading-dependent differential enthalpies and entropies of adsorption.

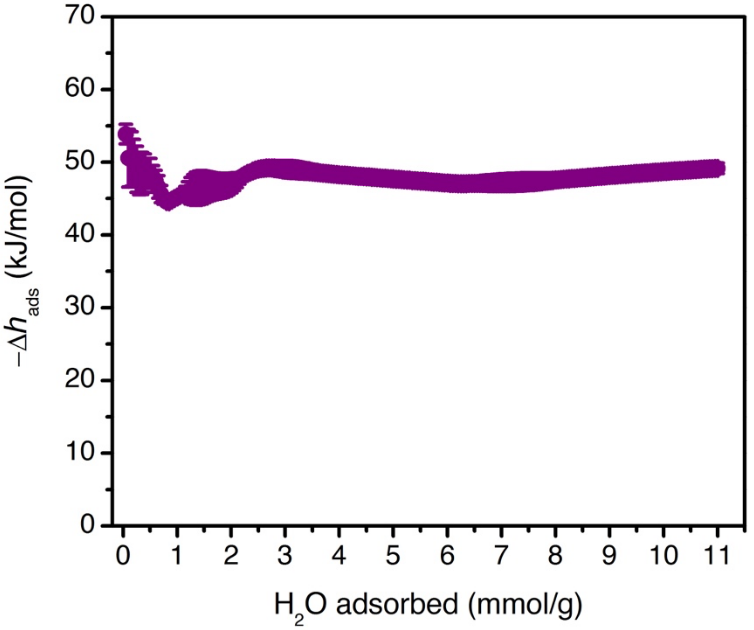

Figure S30. Loading-dependent differential enthalpy of H_2O adsorption for ee-2–Mg_2(dobpdc) calculated from spline interpolation of the H_2O adsorption isotherms at 25, 30, and 40 °C.

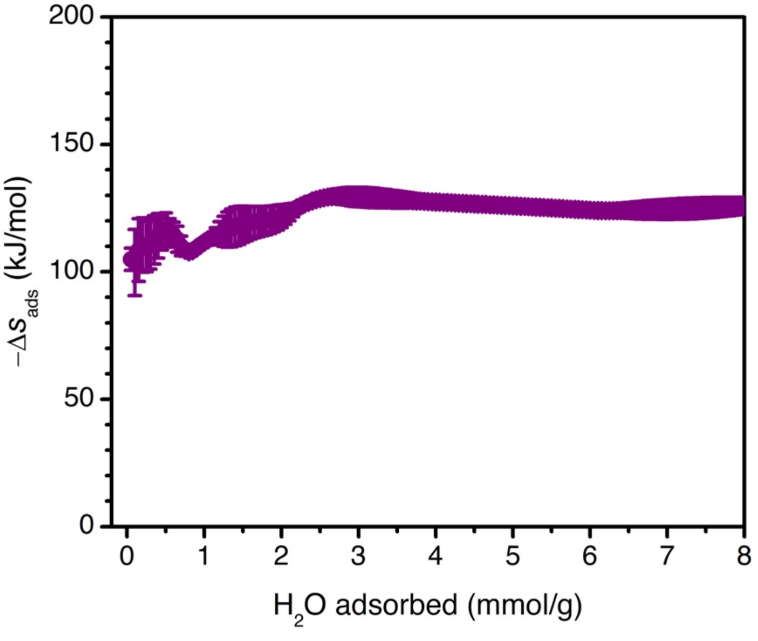

Figure S31. Loading-dependent differential entropy of H_2O adsorption for ee-2–Mg_2(dobpdc) calculated from spline interpolation of the H_2O adsorption isotherms at 25, 30, and 40 °C.

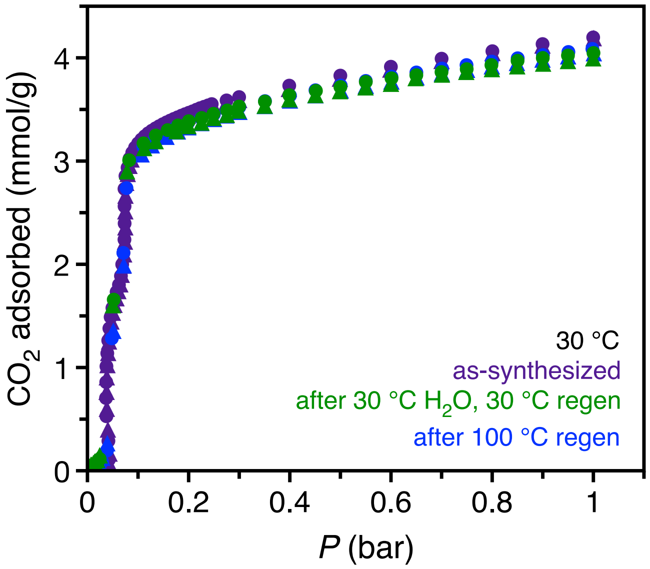

Figure S32. Low-pressure CO_2 adsorption isotherms for ee-2–Mg_2(dobpdc) initially (purple), after collection of a 30 °C H_2O isotherm and regeneration with a turbomolecular pump at 30 °C (green), and after vacuum regeneration at 100 °C (blue). Circles show the as-synthesized powdered material; triangles show binderless pellets prepared by mechanical compaction.

7. Adsorption Isotherms, Fits, and Thermodynamic Data for Zeolite 13X

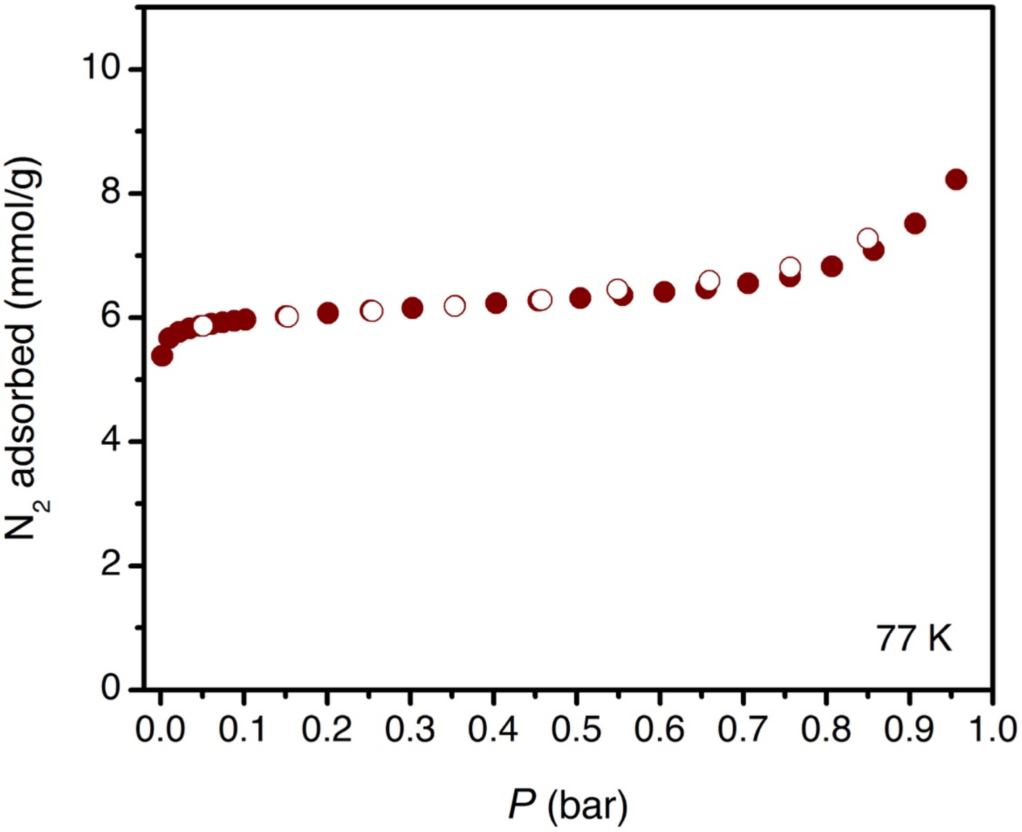

Figure S33. Surface area measurement of zeolite 13X with N_2 at 77 K. Filled circles indicate adsorption; open circles indicate desorption. The Langmuir surface area was calculated as 631 ± 4 m^2/g. A pore volume of 0.24 cm^3/g was calculated from the loading at $P/P_0 = 0.80$.

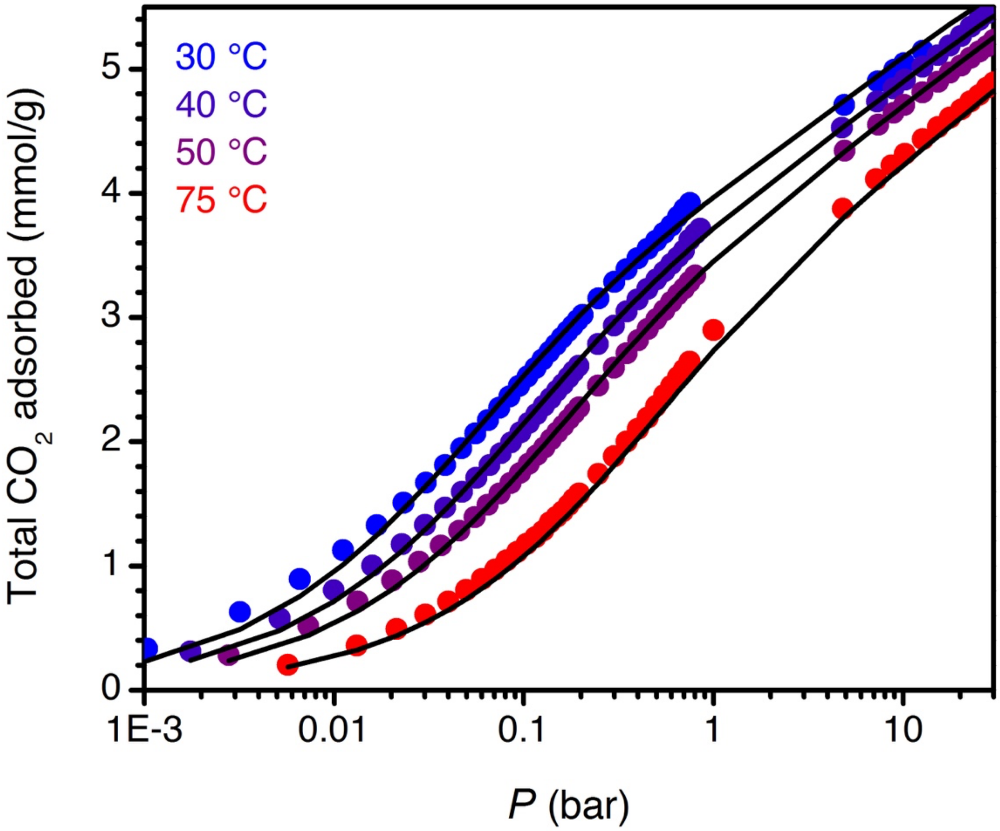

Figure S34. Low- and high-pressure CO_2 adsorption isotherms for zeolite 13X (circles) and corresponding simultaneous dual-site Langmuir–Freundlich fits (lines).

Table S6. Dual-site Langmuir–Freundlich fit parameters for the CO_2 adsorption isotherms of zeolite 13X at 30, 40, 50, and 75 °C (fit simultaneously for all temperatures); $q_{sat,i}$ is the saturation capacity, S_i is the site-specific molar entropy of adsorption, E_i is the site-specific binding energy, and v_i is the Freundlich parameter.

$q_{sat,1}$ (mmol/g)	$-S_1$ (R)	$-E_1$ (kJ/mol)	v_1	$q_{sat,2}$ (mmol/g)	$-S_2$ (R)	$-E_2$ (kJ/mol)	v_2
4.11	9.28	28.4	0.7	2.36	9.99	20.8	0.7

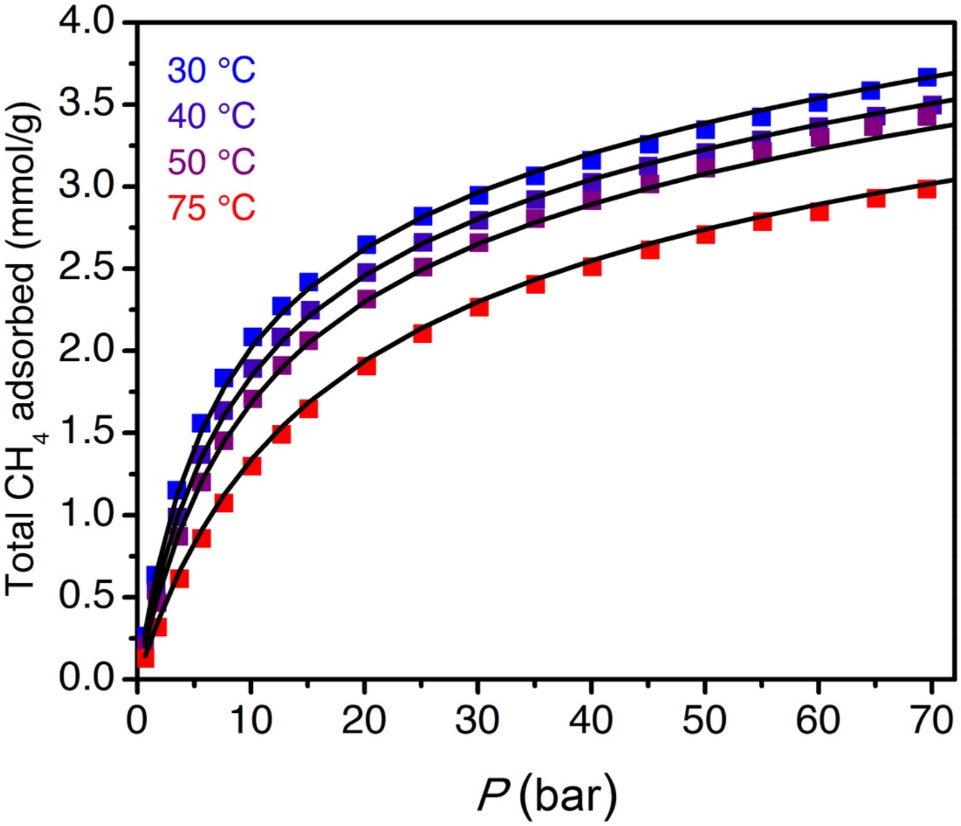

Figure S35. High-pressure CH_4 adsorption isotherms for zeolite 13X (squares) and corresponding simultaneous dual-site Langmuir fits (lines).

Table S7. Dual-site Langmuir fit parameters for the CH_4 adsorption isotherms of zeolite 13X at 30, 40, and 50 °C (fit simultaneously for all temperatures); $q_{sat,i}$ is the saturation capacity, S_i is the site-specific molar entropy of adsorption, E_i is the site-specific binding energy, and R is the gas constant in J/mol·K.

$q_{sat,1}$ (mmol/g)	$-S_1$ (R)	$-E_1$ (kJ/mol)	$q_{sat,2}$ (mmol/g)	$-S_2$ (R)	$-E_2$ (kJ/mol)
3.09	7.93	15.2	2.92	11.2	15.2

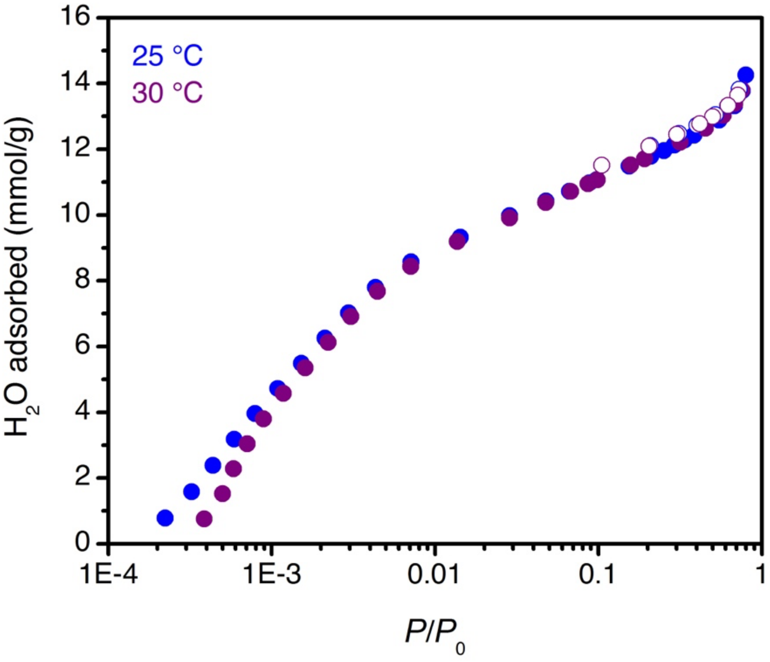

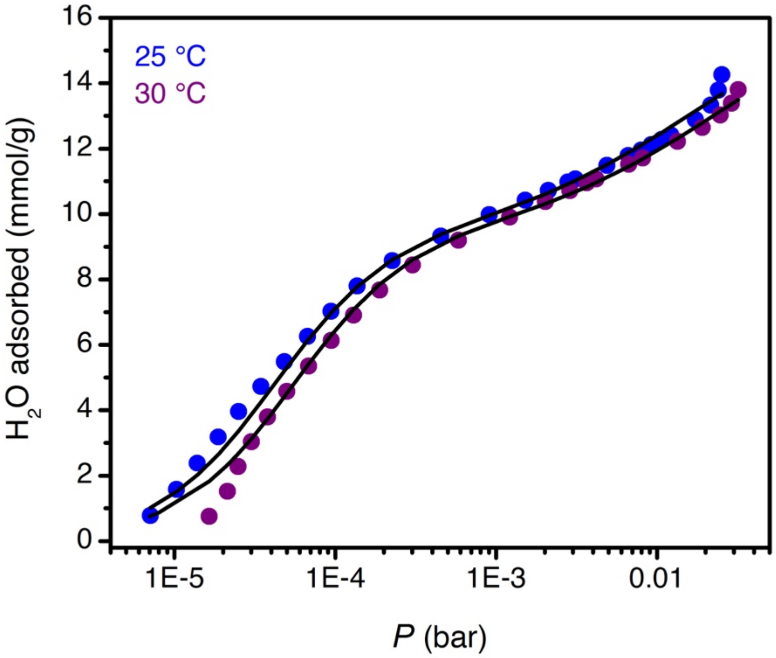

Figure S36. Adsorption (filled circles) and desorption (open circles) H_2O isotherms for zeolite 13X. Data are plotted as a function of both relative pressure (top) and absolute pressure (bottom). Simultaneous dual-site Langmuir Freundlich fits are depicted as black lines in the absolute pressure plot.

Table S8. Dual-site Langmuir–Freundlich fit parameters for the H_2O adsorption isotherms of zeolite 13X at 25 and 30 °C (fit simultaneously); $q_{sat,i}$ is the saturation capacity, S_i is the site-specific molar entropy of adsorption, E_i is the site-specific binding energy, and v_i is the Freundlich parameter.

$q_{sat,1}$ (mmol/g)	$-S_1$ (R)	$-E_1$ (kJ/mol)	v_1	$q_{sat,2}$ (mmol/g)	$-S_2$ (R)	$-E_2$ (kJ/mol)	v_2
9.38	16	49.1	1.2	7.61	18	39.5	0.72

8. Heat Capacity Measurements with Dynamic Scanning Calorimetry

All dynamic scanning calorimetry (DSC) experiments were conducted under 25 mL/min of He using a TA Instruments DSC Q200. Sensor capacitance and resistance were calibrated using factory-provided sapphire disks and ultra-high purity indium. For heat capacity experiments, an additional calibration of the modulated (MDSC) mode[2] was conducted using factory-provided sapphire disks in Tzero™ pans. Cell constants for the MDSC mode were calculated by taking the ratio of the experimental reversing and non-reversing heat capacities to the literature values for sapphire. All MDSC calibration and experimental datasets were conducted with a modulation period of 80 s, an amplitude of 0.75 °C, and a ramp rate of 2 °C/min. Accurate sample masses were obtained by taring the Tzero™ pan on a TGA Q5000, loading the sample into the Tzero™ pan, and activating the sample under flowing N_2 in the TGA furnace. The sample was then transferred to the DSC Q200 in air and reactivated under flowing He within the DSC instrument prior to measurement. Note that the lid of the Tzero™ pan was not completely sealed to allow removal of adsorbed guest molecules during activation within the DSC.

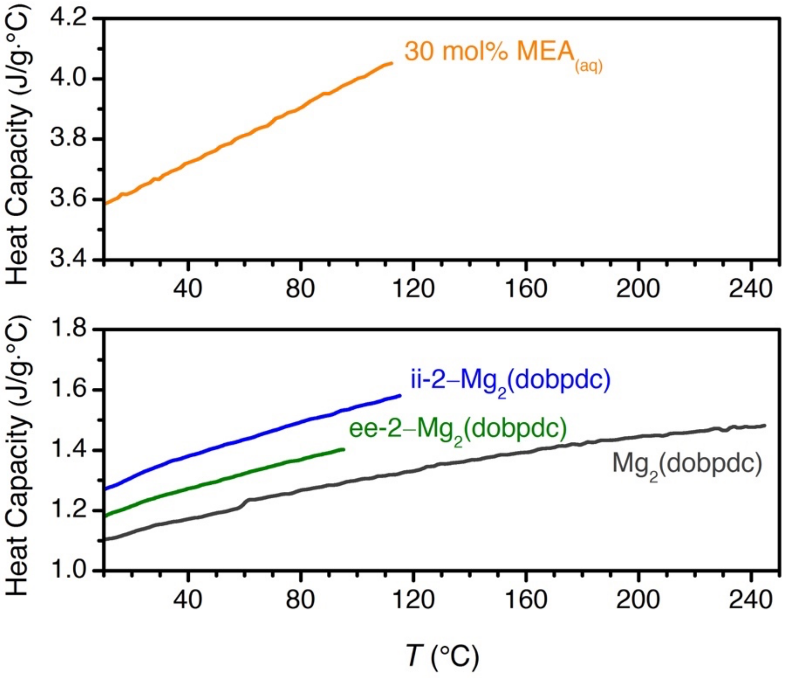

Figure S37. Reported heat capacity for 30 mol% aqueous monoethanolamine (MEA, top),[3] and measured reversible heat capacity for Mg_2(dobpdc) (gray), ee-2–Mg_2(dobpdc) (green), and ii-2–Mg_2(dobpdc) (blue).

9. Kinetics Experiments with Dynamic Scanning Calorimetry

Kinetics experiments with DSC were performed using the same calibration and sample preparation methods discussed in section S8 above. All DSC experiments were performed at atmospheric pressure. After activating the sample under flowing He, the sample was cooled to the specified temperature and switched to a flow of pure CO_2, and the exotherm corresponding to CO_2 adsorption was monitored as a function of time. Time t_0 was selected as the onset of the exotherm. The samples were reactivated at 100 °C under flowing He between each adsorption cycle. For diamine-appended frameworks, the exotherm was found to broaden and flatten as a function of time, consistent with slower CO_2 adsorption kinetics as the experiment temperature approaches the CO_2 adsorption step temperature.

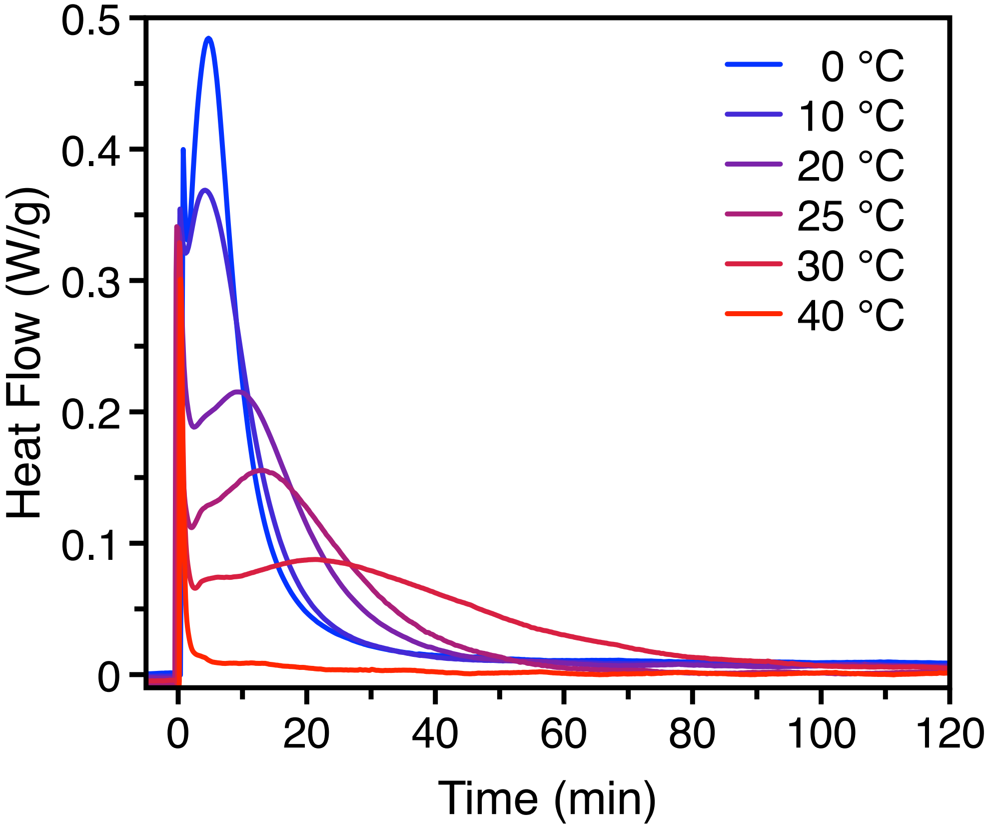

Figure S38. Adsorption kinetics of ii-2–Mg_2(dobpdc) as measured by DSC under a flow of pure CO_2 at atmospheric pressure. Minimal exothermic adsorption was observed at 40 °C, the temperature at which the step position reaches atmospheric pressure for this material.

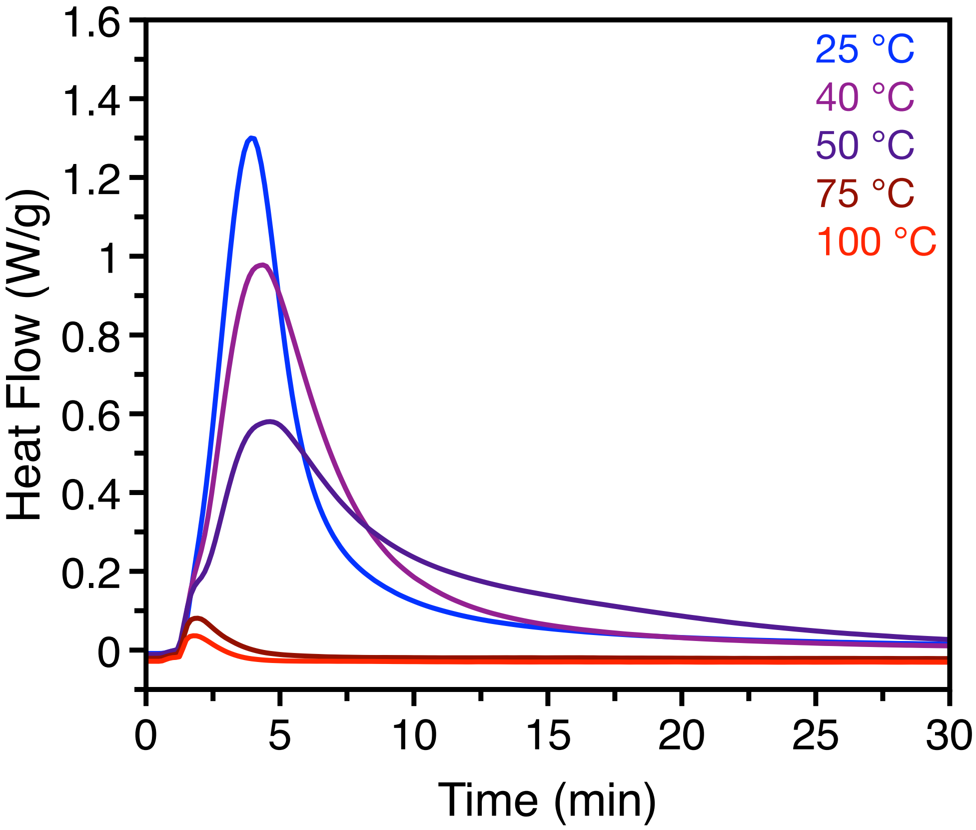

Figure S39. Adsorption kinetics of ee-2–Mg_2(dobpdc) as measured by DSC under a flow of pure CO_2 at atmospheric pressure. Minimal exothermic adsorption was observed at 75 °C, the temperature at which the step position reaches atmospheric pressure for this material.

10. *In Situ* Infrared Spectra for ee-2–Mg_2(dobpdc)

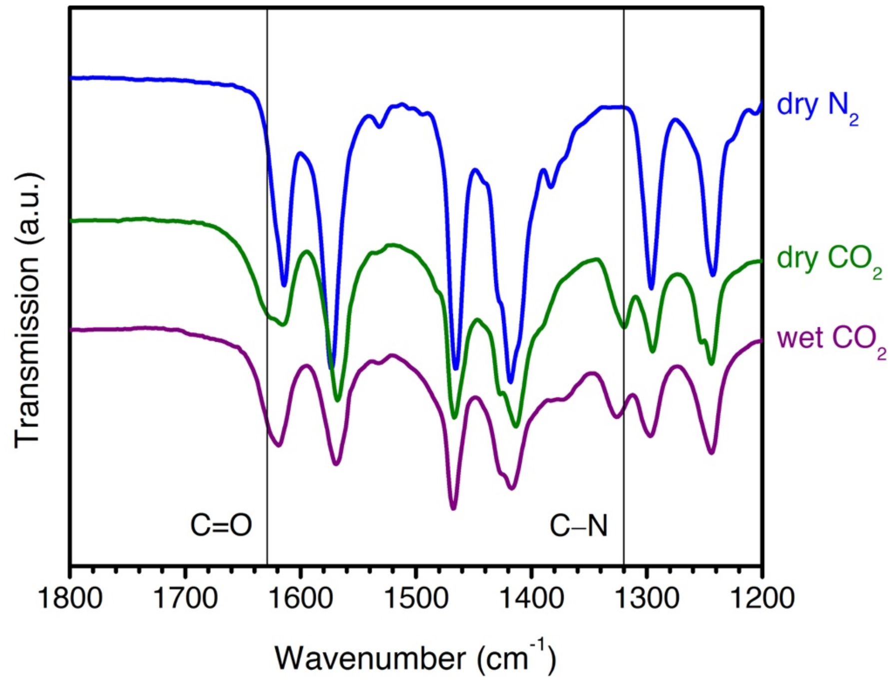

Figure S40. *In situ* infrared spectra at room temperature under N_2 (blue), dry CO_2 (green), and humid CO_2 (purple) for ee-2–Mg2(dobpdc). Gray lines mark the positions of the diagnostic carbamate ν(C=O) (1629 cm^{-1}) and ν(C–N) (~1320 cm^{-1}) bands under dry CO_2.

11. Effect of Humidity on CO_2 Adsorption in ee-2–Mg_2(dobpdc)

Adsorption and desorption isobars were collected with ee-2–Mg_2(dobpdc) for a range of CO_2 concentrations in N_2 under both dry and humid conditions at atmospheric pressure. For humid isobars, the inlet stream to the TGA furnace was humidified by flowing through two room-temperature (~20 °C) water bubblers in series. The estimated water content was 1.3%, as determined by the pressure at which the same quantity of water was adsorbed in the single-component 40 °C H_2O isotherm and the humid N_2 isobar (simulating a H_2O isobar). This estimated water content is equivalent to that determined for the same humid TGA apparatus in a previous report.[4]

For all CO_2 concentrations, an increase in the isobaric step temperature was observed under humid conditions. The higher step temperature (equivalent to a lower isothermal step pressure) under humid conditions suggests an increase in the thermodynamic driving force for CO_2 adsorption in the presence of H_2O, consistent with previous reports.[5,6] However, H_2O may also enhance the kinetics of CO_2 adsorption by facilitating proton transfer. We are continuing to investigate the thermodynamics and kinetics of CO_2 and H_2O co-adsorption in ongoing work. We note that for humid isobars, continued mass increase was observed during the desorption branch of the isobar, suggesting incomplete equilibration of the total mass of CO_2 and H_2O adsorbed with the temperature ramp rates used for these experiments.

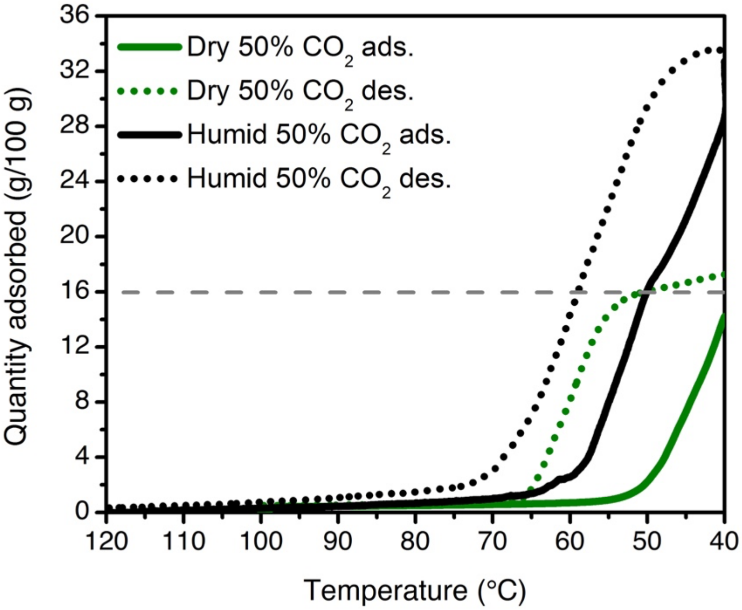

Figure S41. Dry 50% CO_2 in N_2 adsorption (solid green) and desorption (dotted green) isobars, and humid 50% CO_2 in N_2 adsorption (solid black) and desorption (dotted black) isobars, for ee-2–Mg_2(dobpdc). The material was activated at 120 °C under flowing dry (green) or humid (black) N_2 for 20 min. Isobars were collected at atmospheric pressure using a ramp rate of 1 °C/min. The gray dashed line indicates the expected adsorption capacity corresponding to 1 CO_2 per diamine.

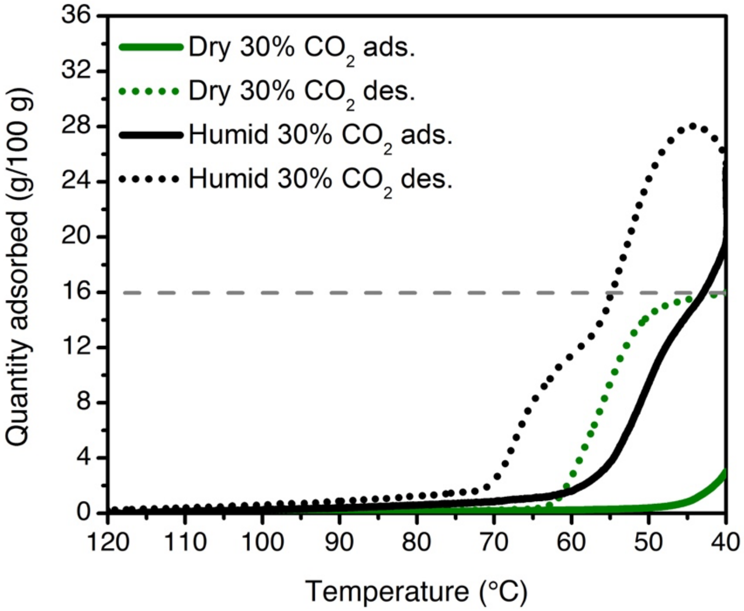

Figure S42. Dry 30% CO_2 in N_2 adsorption (solid green) and desorption (dotted green) isobars, and humid 30% CO_2 in N_2 adsorption (solid black) and desorption (dotted black) isobars, for ee-2–Mg_2(dobpdc). The material was activated at 120 °C under flowing dry (green) or humid (black) N_2 for 20 min. Isobars were collected at atmospheric pressure using a ramp rate of 1 °C/min. The gray dashed line indicates the expected adsorption capacity corresponding to 1 CO_2 per diamine.

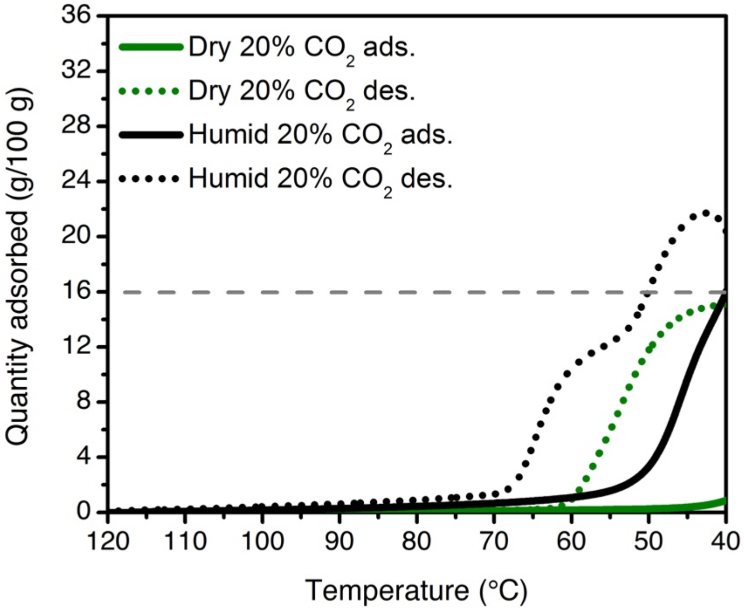

Figure S43. Dry 20% CO_2 in N_2 adsorption (solid green) and desorption (dotted green) isobars, and humid 20% CO_2 in N_2 adsorption (solid black) and desorption (dotted black) isobars, for ee-2–Mg_2(dobpdc). The material was activated at 120 °C under flowing dry (green) or humid (black) N_2 for 20 min. Isobars were collected at atmospheric pressure using a ramp rate of 1 °C/min. The gray dashed line indicates the expected adsorption capacity corresponding to 1 CO_2 per diamine.

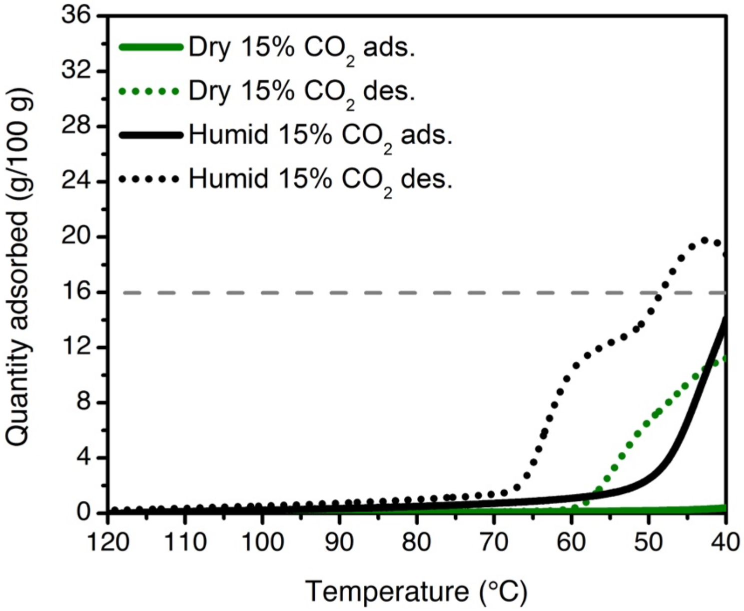

Figure S44. Dry 15% CO_2 in N_2 adsorption (solid green) and desorption (dotted green) isobars, and humid 15% CO_2 in N_2 adsorption (solid black) and desorption (dotted black) isobars, for ee-2–Mg_2(dobpdc). The material was activated at 120 °C under flowing dry (green) or humid (black) N_2 for 20 min. Isobars were collected at atmospheric pressure using a ramp rate of 1 °C/min. The gray dashed line indicates the expected adsorption capacity corresponding to 1 CO_2 per diamine.

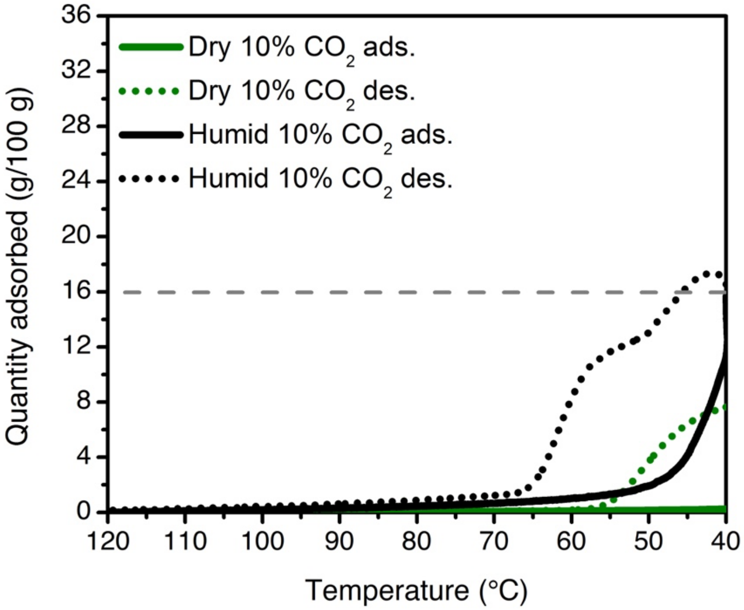

Figure S45. Dry 10% CO_2 in N_2 adsorption (solid green) and desorption (dotted green) isobars, and humid 10% CO_2 in N_2 adsorption (solid black) and desorption (dotted black) isobars, for ee-2–Mg_2(dobpdc). The material was activated at 120 °C under flowing dry (green) or humid (black) N_2 for 20 min. Isobars were collected at atmospheric pressure using a ramp rate of 1 °C/min. The gray dashed line indicates the expected adsorption capacity corresponding to 1 CO_2 per diamine.

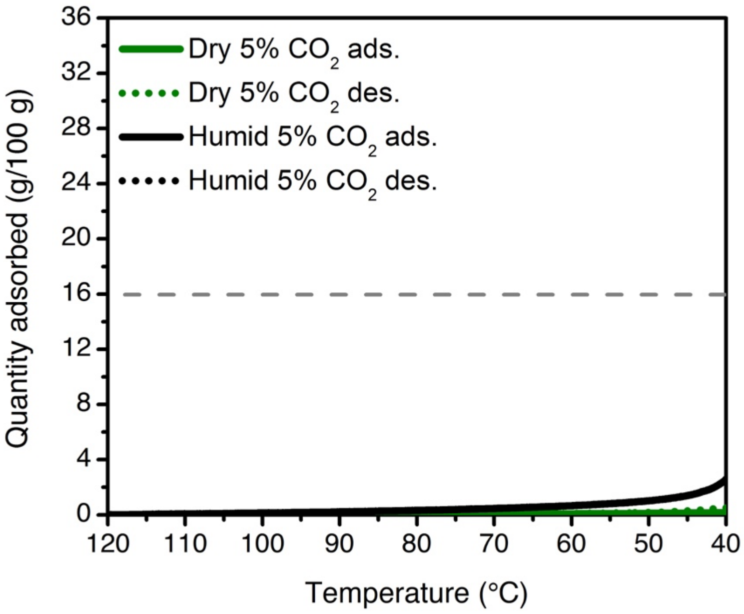

Figure S46. Dry 5% CO_2 in N_2 adsorption (solid green) and desorption (dotted green) isobars, and humid 5% CO_2 in N_2 adsorption (solid black) and desorption (dotted black) isobars, for ee-2–Mg_2(dobpdc). The material was activated at 120 °C under flowing dry (green) or humid (black) N_2 for 20 min. Isobars were collected at atmospheric pressure using a ramp rate of 1 °C/min. The gray dashed line indicates the expected adsorption capacity corresponding to 1 CO_2 per diamine.

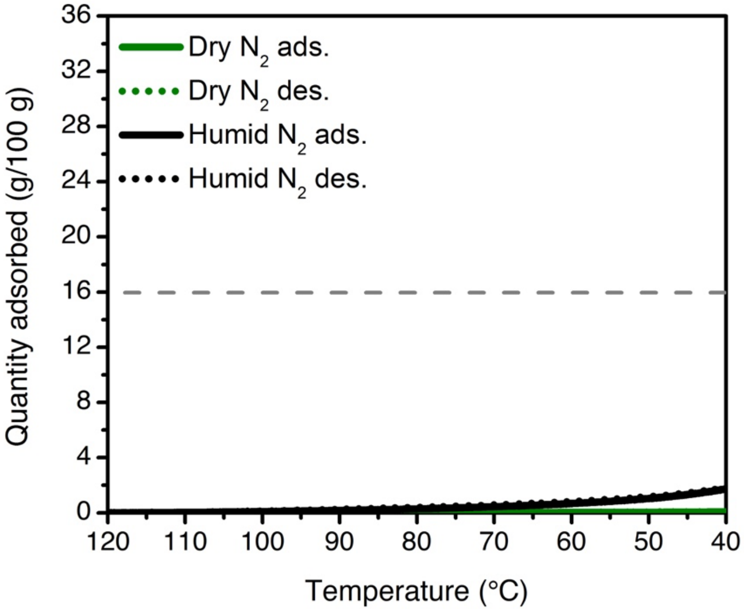

Figure S47. Dry N_2 adsorption (solid green) and desorption (dotted green) isobars, and humid N_2 adsorption (solid black) and desorption (dotted black) isobars, for ee-2–Mg_2(dobpdc). The material was activated at 120 °C under flowing dry (green) or humid (black) N_2 for 20 min. Isobars were collected at atmospheric pressure using a ramp rate of 1 °C/min. The gray dashed line indicates the expected adsorption capacity corresponding to 1 CO_2 per diamine.

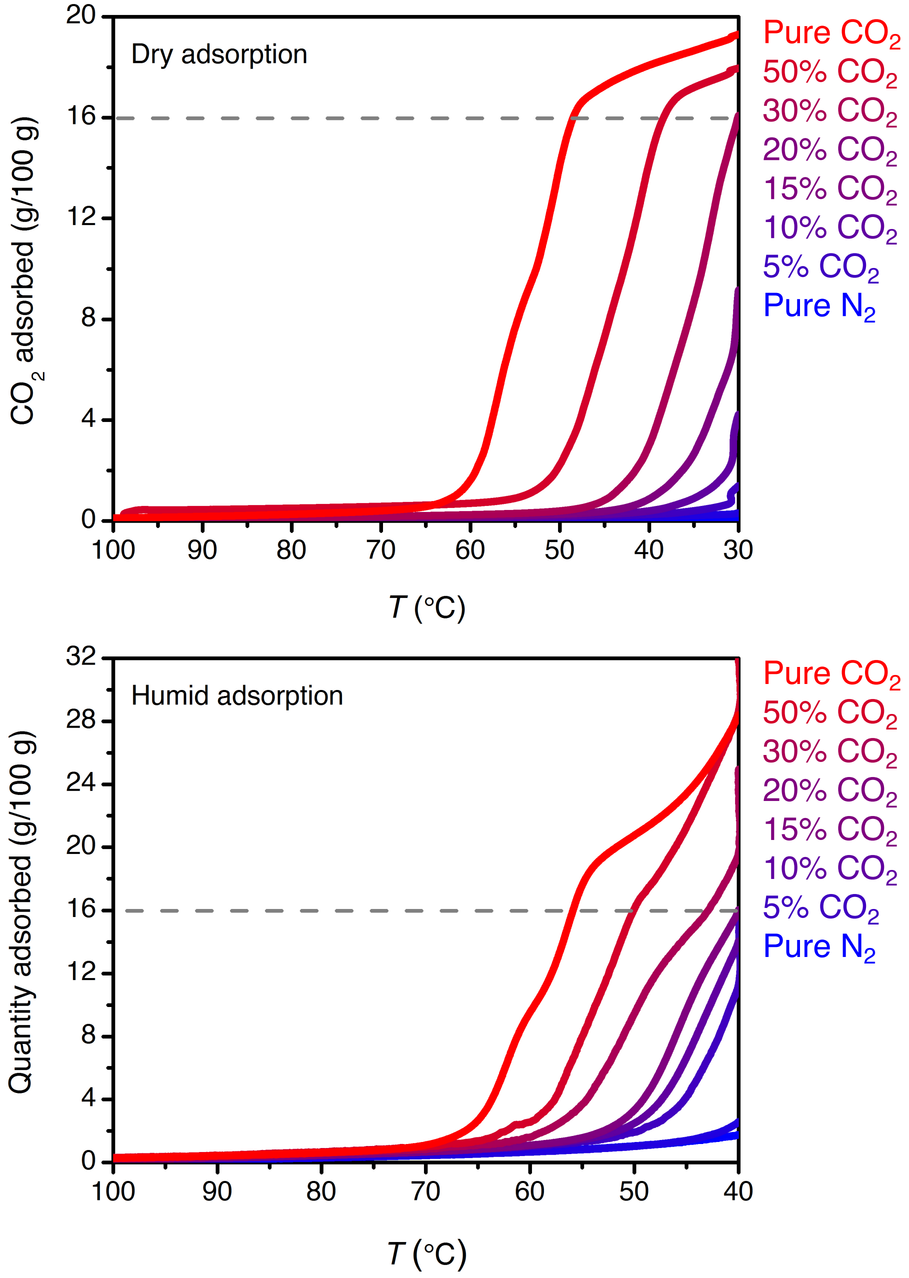

Figure S48. Full series of dry (top) and humid (bottom) adsorption isobars for pure CO_2, CO_2/N_2 mixtures, and pure N_2 at atmospheric pressure (note different temperature scales on horizontal axes). A temperature ramp rate of 1 °C/min was used for all experiments.

12. Predicting Breakthrough Curves from Step-Shaped Adsorption Isotherms

Simple graphical approaches can be used to predict breakthrough profiles directly from adsorption isotherms. An excellent review of this topic is provided by Helfferich and Carr,[7] and the key points of this analysis are reproduced here. This analysis is also included in a parallel study by our group regarding CO_2 capture from the emissions of natural gas-fired power plants.[6]

To relate isotherms and elution profiles, the primary quantity of interest is the velocity v_{c_i} of a given concentration c_i of solute i as it flows through the adsorption column. This concentration velocity is defined as

$$\boldsymbol{v_{c_i} \equiv \left(\frac{\partial z}{\partial t}\right)_{c_i}}, \qquad \text{(S4)}$$

where z is the linear distance in the direction of flow, and t is time. Neglecting axial dispersion, ideal plug flow under isotherm conditions gives the following equation for conservation of mass:

$$\boldsymbol{\frac{\rho}{\varepsilon}\left(\frac{\partial q_i}{\partial t}\right)_z + \left(\frac{\partial c_i}{\partial t}\right)_z + v^0\left(\frac{\partial c_i}{\partial z}\right)_t = 0} \qquad \text{(S5)}$$

Here, v^0 is the velocity of the moving-phase flow, q_i is the adsorbent loading, ρ is the bulk density of the adsorbent, and ε is the fractional void volume of the adsorbent bed. The resulting "wave equation" for the concentration velocity is thus

$$\boldsymbol{v_{c_i} = \frac{v^0}{\left(1+\frac{\rho}{\varepsilon}\right)\left(\frac{\partial q_i}{\partial c_i}\right)_z}} \qquad \text{(S6)}$$

If local equilibrium is further assumed, the adsorbent loading becomes solely a function of concentration, and the partial differential can be replaced by the corresponding total differential:

$$\boldsymbol{v_{c_i} = \frac{v^0}{\left(1+\frac{\rho}{\varepsilon}\right)\left(\frac{\mathrm{d}q_i}{\mathrm{d}c_i}\right)_z}} \qquad \text{(S7)}$$

Therefore, the concentration velocity is inversely proportional to $\mathrm{d}q_i/\mathrm{d}c_i$, which is the slope of the tangent to the equilibrium adsorption isotherm at the corresponding concentration c_i. In other words, under local equilibrium, *the "natural" wave velocity is lower at concentrations where the isotherm is steeper*. With this knowledge, the propagation of adsorption and desorption waves is straightforward to predict for simple linear, Type I, and Type III isotherms, as illustrated in Figure S49 below.

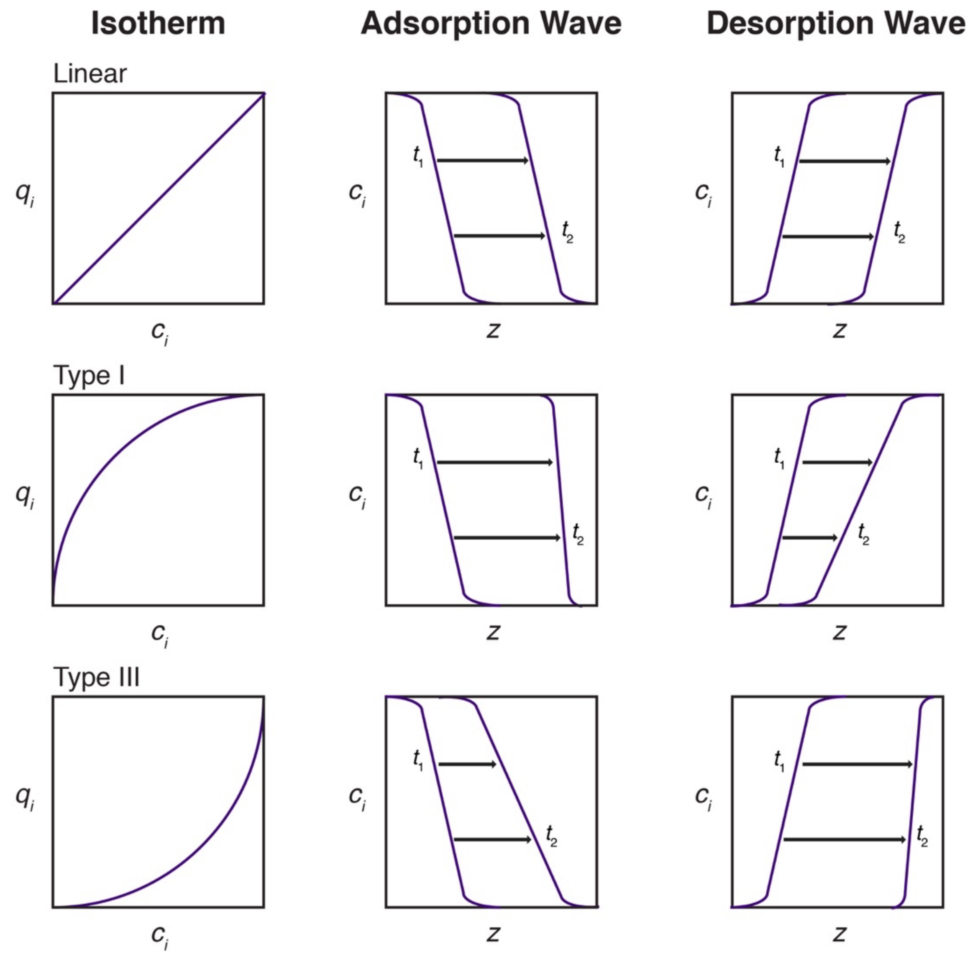

Figure S49. Propagation of adsorption and desorption waves for linear (top), Type I (middle), and Type III (bottom) isotherms under ideal conditions. The left column shows the isotherm profile as loading (q_i) vs. concentration (c_i). The center and right columns show the propagation of the adsorption and desorption waves, respectively, as c_i vs. distance z along the column for a wave initially diffuse at t_1 to a later time t_2. Figure adapted from the work of Helfferich and Carr.[7]

For linear isotherms, the slope of the isotherm is constant, and thus the adsorption and desorption waves propagate through the bed unchanged under ideal conditions. For Type I isotherms, higher concentrations, where the isotherm slope is shallower, move through the bed faster than lower concentrations. On adsorption, this results in a wave that sharpens to a “shock,” or discontinuity, while on desorption, the wave broadens as it travels. Similarly, for adsorption Type III isotherm, lower concentrations move faster than higher concentrations, and the adsorption wave spreads as it moves through the column.

More complex “composite” waves may be generated in the case of isotherms with inflection points. A simple graphical approach known as “Golden’s rule,” or alternatively the “string” or “rubber band” rule, can be used to predict the shape of the breakthrough profile directly from an isotherm of arbitrary shape.[7–13] In this method, an operating curve is constructed from an imaginary rubber band stretched between the initial state (typically, no adsorbate) and the feed state (here, 10% CO_2). For adsorption, the rubber band operating curve falls below the isotherm, while for desorption, it falls above it. In regions where the rubber band is stretched tightly between individual points of contact with the isotherm, compressive waves, or "shocks" are generated in the breakthrough profile. In regions where the rubber band instead runs along the isotherm, dispersive waves are generated. As a result, inflection points in isotherms often lead to multi-moment breakthrough profiles containing both shocks and waves, a schematic of which is shown in Figure 2 of the main text. Importantly, in most cases of interest for diamine-appended frameworks with step-shaped isotherms, this behavior results in an intuitive conclusion: once the CO_2 partial pressure in the bed drops below the step pressure, the cooperative adsorption mechanism is no longer active, and thus *CO_2 at concentrations below the step pressure "slips" through the bed*. Hefti, Joss and coworkers first discussed the importance of considering CO_2 slip for diamine-appended frameworks in a 2016 modeling study,[11] and Darunte and coworkers[13] recently demonstrated CO_2 slip experimentally in breakthrough experiments targeting direct air capture with mmen–Mg_2(dobpdc) (mmen = *N,N′*-dimethylethylenediamine).

In the present study, "shock–wave–shock" breakthrough profiles were observed for CO_2 with dry mixtures simulating crude natural gas streams, but upon incorporation of humidity, single-shock breakthrough profiles were observed under the same conditions. This favorable result enables significant improvements in capture rate under the more realistic H_2O-containing streams. As discussed in the main text, we attribute this enhanced performance to preferential stabilization of the CO_2-bound phase in the presence of water, as reflected in the higher isobaric step temperatures under humid CO_2-containing streams (Figure S41 to Figure S48). This is consistent with a lower effective step pressure in the CO_2 isotherm in the presence of water. The single-shock breakthrough profiles therefore suggest that water reduces the step pressure and/or modifies the pre-step region of the isotherm such that the operating curve no longer intersects the isotherm (main text Figure 10). These results are consistent with a parallel study by our group investigating CO_2 capture from simulated natural gas flue emissions with a diamine-appended metal–organic framework.[6]

13. Additional Experimental Details for Breakthrough Measurements

Breakthrough experiments were conducted with the adsorbent column pre-equilibrated under flowing He unless otherwise noted. To begin the experiment, He flow to the column was stopped as a flow of simulated natural gas was introduced. For quantitative experiments, following complete breakthrough of CO_2, the capacity of each gas (q_i, mmol/g) was determined using the following equation:

$$q_i = \left[\frac{Q}{22.414\frac{cc_{STP}}{mmol}} \int_0^t \left(1 - \frac{F_i}{F_{0,i}}\right) dt - \varepsilon V \left(\frac{y_i P}{RT}\right)\right] \left(\frac{y_i}{m}\right) \qquad \text{(S8)}$$

Here, Q is the average total mass flow rate in sccm, t is the corrected time in min, F_i is the molar flow rate of species i at time t, $F_{0,i}$ is the inlet molar flow rate of species i, ε is the interparticle void fraction, V is the volume of pelletized adsorbent in cm^3, y_i is the mole fraction of species i, P is the total pressure, R is the universal gas constant, T is the column temperature in K, and m is the mass of adsorbent. The interparticle void fraction ε is calculated as

$$\varepsilon = 1 - \frac{\rho_{bulk}}{\rho_{particle}} \qquad \text{(S9)}$$

where ρ_{bulk} is the bulk density in kg/m^3, calculated as m/V, and $\rho_{particle}$ is the particle density in kg/m^3 and is estimated as 1000 kg/m^3 for diamine-appended frameworks.

For the custom dry breakthrough apparatus (Figure S51), reported data were corrected for the system deadtime, which was determined by running breakthrough experiments with an empty column. A representative deadtime of 392 s was determined for experiments at 70 bar under 300 sccm of 10% CO_2 in CH_4. An insulated clamshell furnace (Applied Test Systems) was used to control the bed temperature, and a manual back-pressure regulator was used to control the bed pressure. The internal bed temperature was measured with thermocouples at 3" and 9" along the 12" column. The composition of the outlet stream was monitored using an OmniStar mass spectrometer. A standard flow rate of 300 sccm was supplied using a Brooks flow controller. The flow rate of the outlet stream was measured using a thermal mass flow meter calibrated to CH_4, and the recorded values were corrected for the true composition at each time point using the viscosity calculated from the Wilke model. Flow, pressure, and temperature data were recorded every 30 s until breakthrough and every several minutes thereafter until complete bed saturation was observed. Diamine-appended frameworks were activated at 100 °C under house vacuum (~0.15 bar) for 12 h between runs unless specified otherwise.

For qualitative dry and humid breakthrough experiments at 7 and 50 bar, a customized PSA-1000 apparatus from L&C Science was used. Additional information is available from the manufacturer.[14] The outlet composition was monitored using a mass spectrometer. Diamine-appended frameworks were activated at 100 °C with a rotary vacuum pump (~0.02 mbar) for 12 h between runs unless specified otherwise. Zeolite 13X was activated with a rotary vacuum pump (~0.02 mbar) for 2 h at 100 °C and 8 h at 300 °C between runs unless specified otherwise.

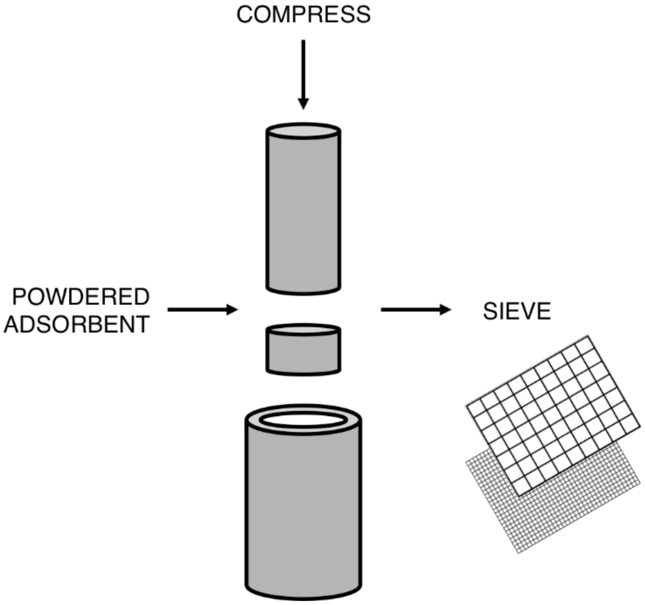

Figure S50. Schematic of compression method used to prepare pelletized adsorbent from microcrystalline powder.

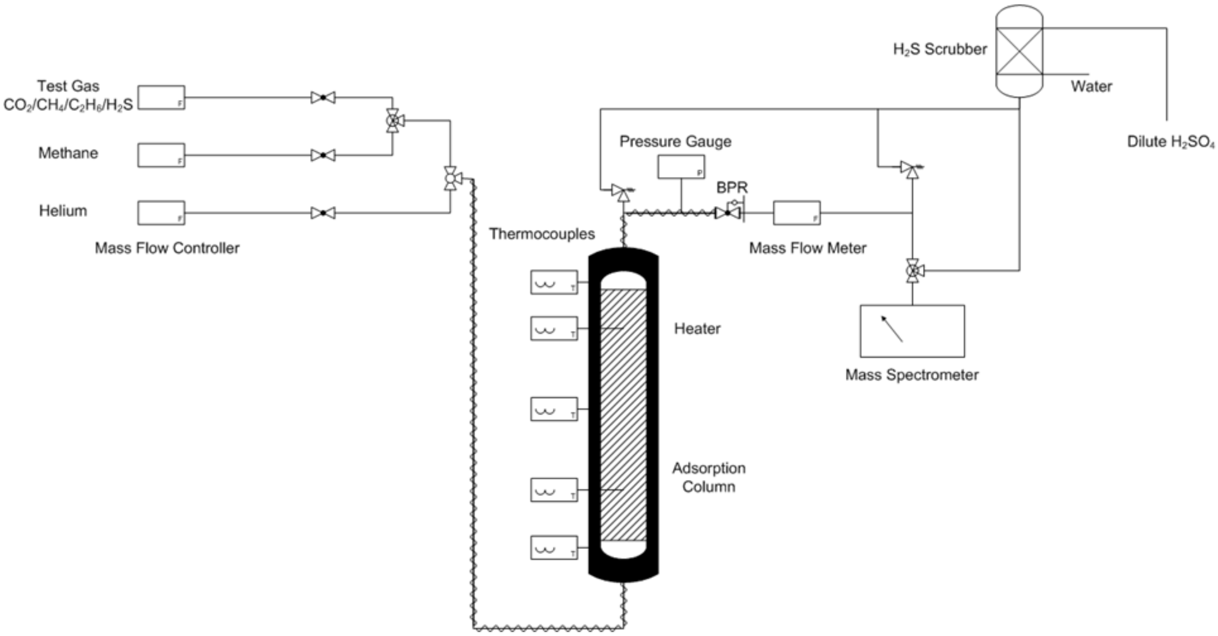

Figure S51. Schematic of home-built breakthrough apparatus used for quantitative breakthrough experiments with dry gas streams. The column pressure was controlled using a back-pressure regulator (BPR). While the system is equipped with an H_2S scrubber, H_2S testing capabilities were not yet operational at the time of writing.

14. Additional Breakthrough Experiments with ii-2–Mg_2(dobpdc)

Table S9. Summary of breakthrough results for ii-2–Mg_2(dobpdc) with 10% CO_2 in CH_4. A capacity of 3.3 mmol/g corresponds to adsorption of 1 CO_2 per diamine. The CO_2 exhaustion capacities (integrated over the full breakthrough curve) are reported with an estimated error of ±0.3 mmol/g. All experiments listed below were performed on the home-built breakthrough apparatus. Due to the high degree of uncertainty for CH_4 breakthrough capacity resulting from the short CH_4 breakthrough times for these experiments, methane loss is not reported here, but this will be critical to quantify in future work.

T **(°C)**	***P*** P_{total} **(bar)**	**Flow rate (sccm)**	**Predicted CO_2 slip (mol %, bar)**	**Observed CO_2 slip (mol %, bar)**	**Observed CH_4 purity (mol %)**	**CO_2 exhaustion capacity (mmol/g)**
30	70	300	<1%, <0.7	3%, 2	97	3.3
50	70	300	~2.2%, ~1.5	6%, 4	94	3.4
30	35	300	~1%, ~0.7	6%, 2	94	3.8

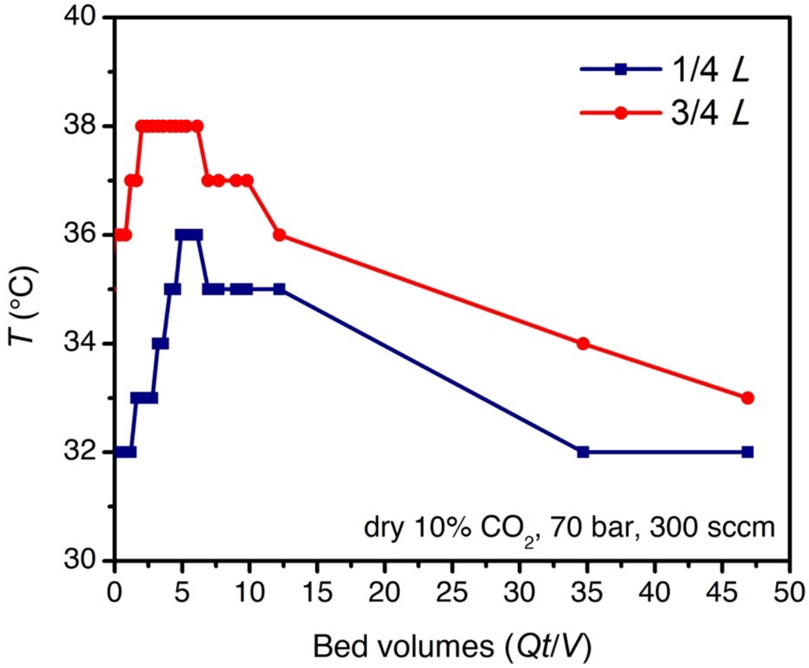

Figure S52. Temperature profile for the breakthrough experiment with ii-2–Mg_2(dobpdc) shown in main text Figure 4.

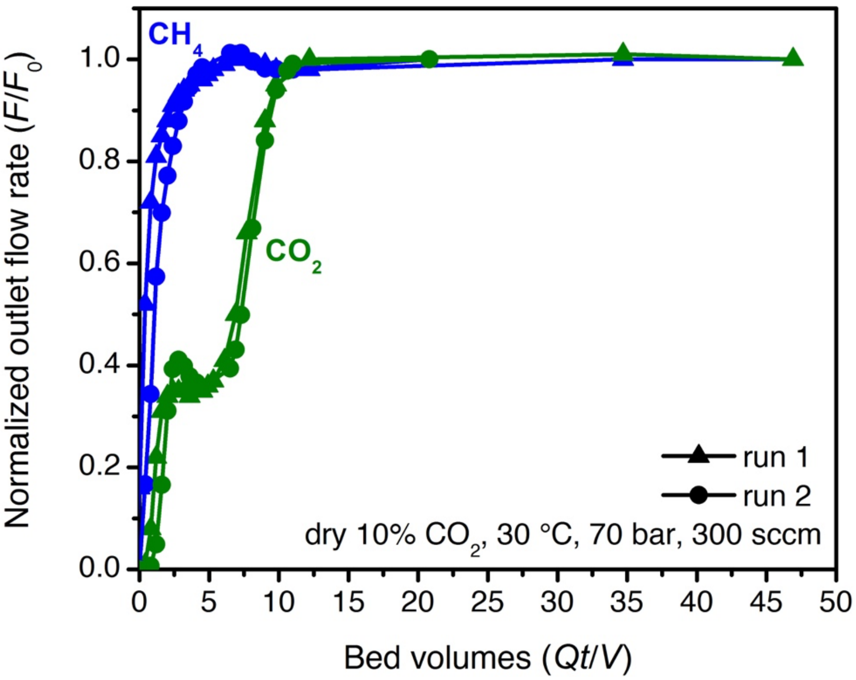

Figure S53. Duplicate breakthrough experiments for ii-2–Mg_2(dobpdc) under 300 sccm of dry 10% CO_2 in CH_4 at 30 °C and 70 bar. The data shown for run 1 are the same as those shown in the main text.

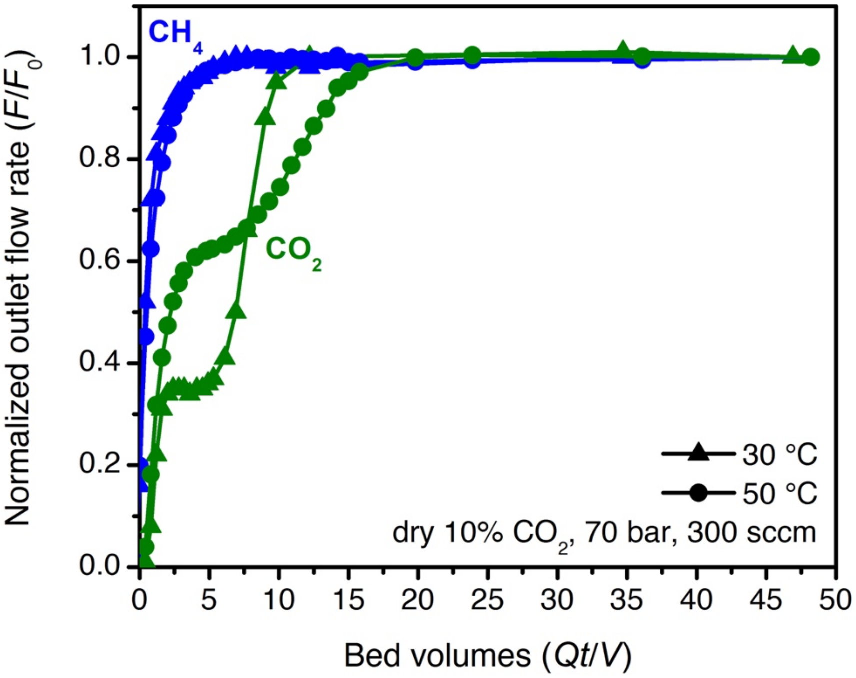

Figure S54. Breakthrough curves for ii-2–Mg_2(dobpdc) at 30 °C (triangles) and 50 °C (circles) under 300 sccm of dry 10% CO_2 in CH_4 at 70 bar. The data shown for 30 °C are the same as those shown in the main text.

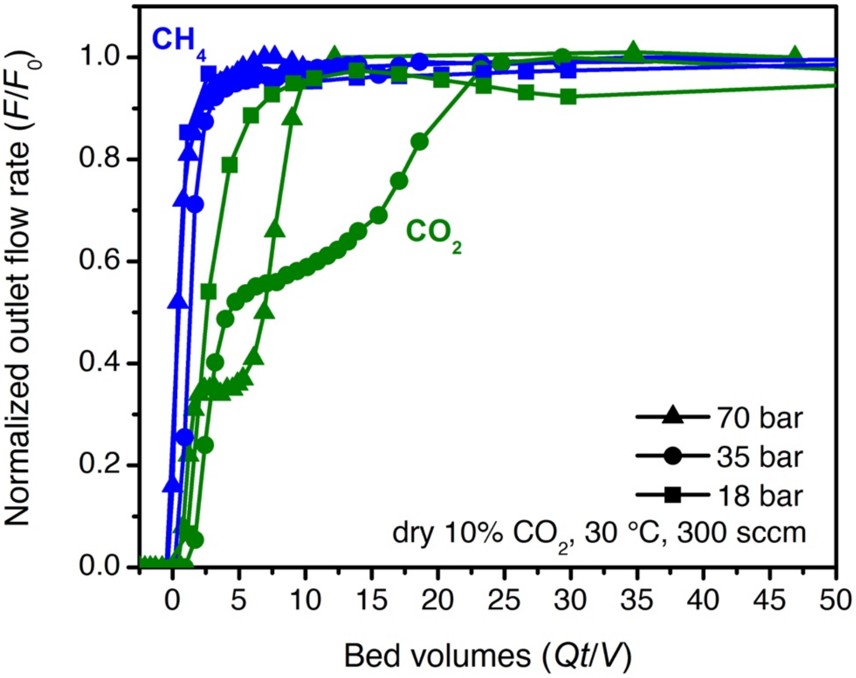

Figure S55. Breakthrough curves for ii-2–Mg_2(dobpdc) at 70 bar (triangles), 35 bar (circles), and 18 bar (squares) under 300 sccm of dry 10% CO_2 in CH_4 at 30 °C. The data shown for 70 bar are the same as those shown in the main text.

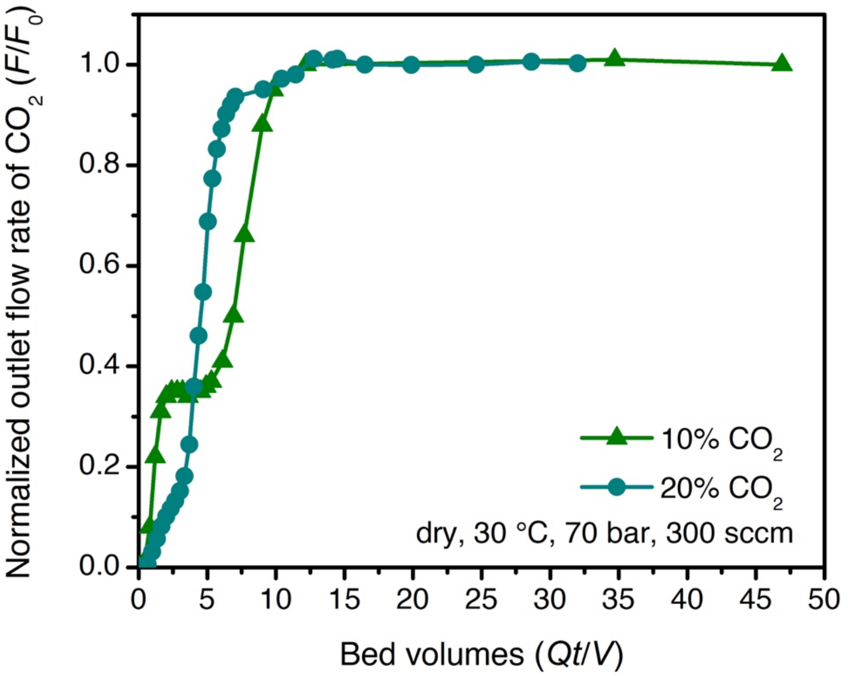

Figure S56. Breakthrough curves for ii-2–Mg_2(dobpdc) under 300 sccm of varying inlet concentrations of CO_2 in CH_4 at 70 bar and 30 °C. The data shown for 10% CO_2 are the same as those shown in the main text. For the experiment with 20% CO_2 in CH_4, the column was pre-equilibrated under pure CH_4 rather than He.

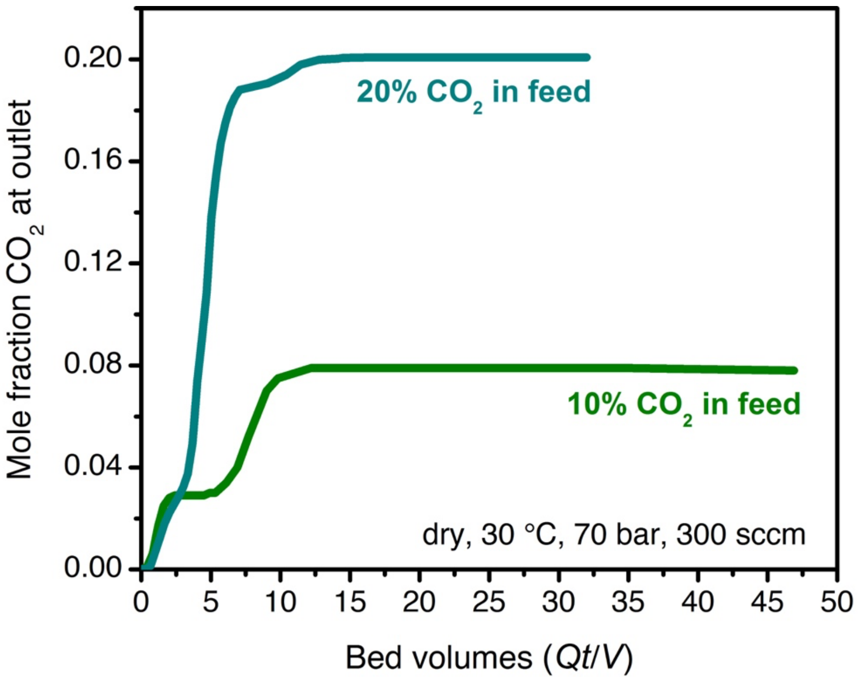

Figure S57. Mole fraction data from the breakthrough experiment shown in Figure S56.

15. Additional Breakthrough Experiments with ee-2–Mg_2(dobpdc)

Table S10. Summary of breakthrough results for ee-2–Mg_2(dobpdc) with 10% CO_2 in CH_4. A capacity of 3.6 mmol/g corresponds to adsorption of 1 CO_2 per diamine. For quantitative experiments at 70, 35, and 1 bar, CO_2 exhaustion capacities (integrated over the full breakthrough curve) are reported with an estimated error of ±0.3 mmol/g. Quantitative experiments were performed on the home-built breakthrough apparatus. The qualitative experiment at 7 bar was performed on the customized L&C PSA instrument. Due to the high degree of uncertainty for CH_4 breakthrough capacity resulting from the short CH_4 breakthrough times for these experiments, methane loss is not reported here, but this will be critical to quantify in future work.

T (°C)	P_{total} (bar)	Flow rate (sccm)	Predicted CO_2 slip (mol %, bar)	Observed CO_2 slip (mol %, bar)	Observed CH_4 purity (mol %)	CO_2 exhaustion capacity (mmol/g)
30	70	300	0.09%, 0.06	0.4%, 0.3	99.6	4.2
30	35	300	0.2%, 0.06	0.8%, 0.3	99.2	4.9
30	7	300	0.9%, 0.06	4%, 0.3	96.0	not calculated
30	1	300	6%, 0.06	5%, 0.05	95.0	1.6

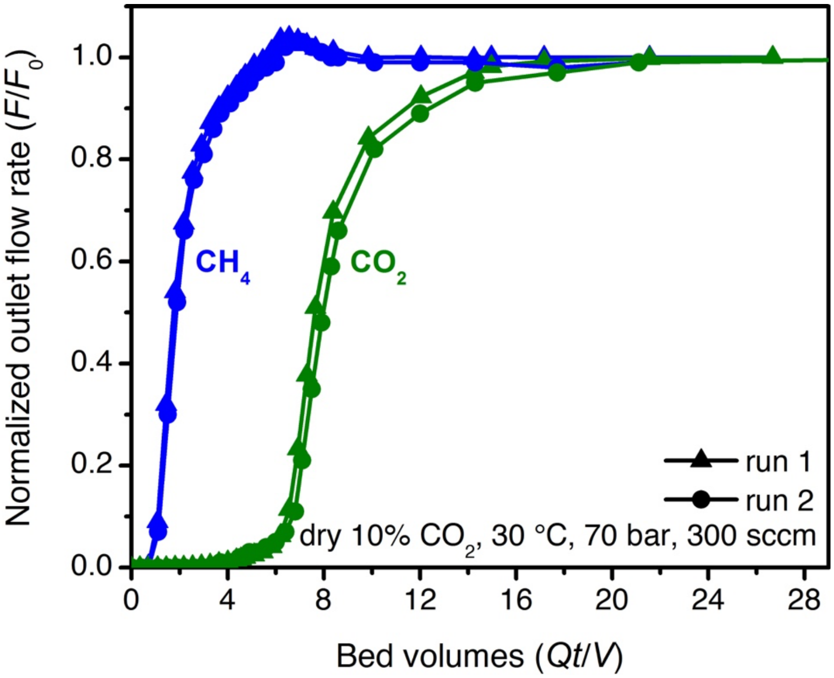

Figure S58. Duplicate breakthrough experiments for ee-2–Mg_2(dobpdc) under 300 sccm of dry 10% CO_2 in CH_4 at 30 °C and 70 bar. The data shown for run 1 are the same as those shown in the main text.

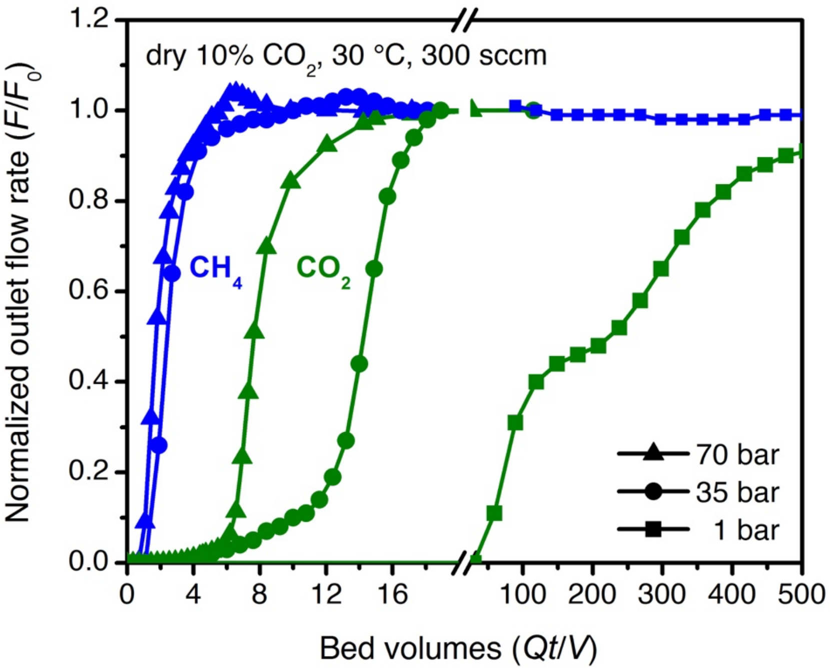

Figure S59. Breakthrough curves for ee-2–Mg_2(dobpdc) at 70 bar (triangles), 35 bar (circles), and 1 bar (squares) under 300 sccm of dry 10% CO_2 in CH_4 at 30 °C. The data shown for 70 bar are the same as those shown in the main text.

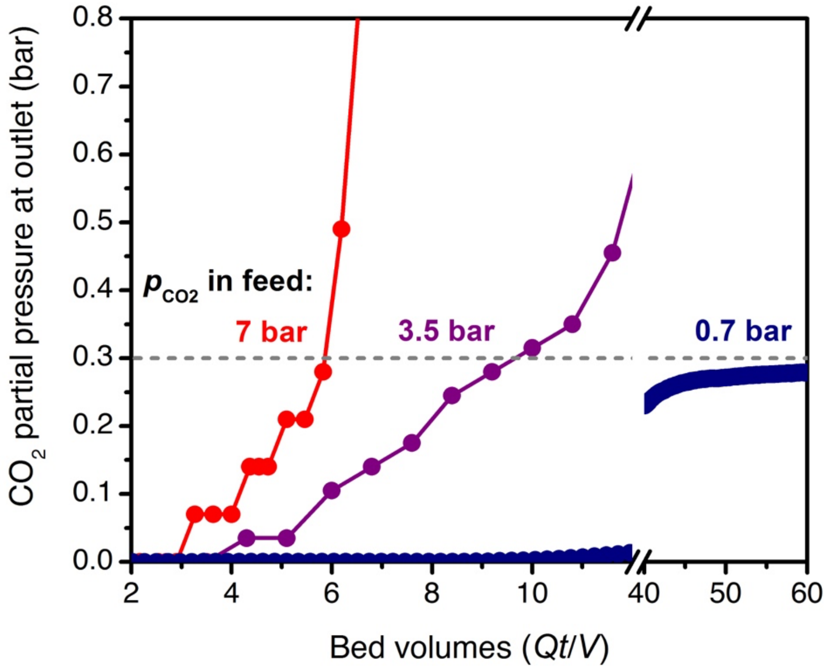

Figure S60. Breakthrough curves for ee-2–Mg_2(dobpdc) with 300 sccm of dry 10% CO_2 at 30 °C and a total pressure of 70 bar (red), 35 bar (purple), and 7 bar (blue). Experiments are plotted in terms of CO_2 partial pressure at the outlet vs bed volumes to demonstrate the consistent slip of ~0.3 bar of CO_2 (gray dashed line) prior to full breakthrough.

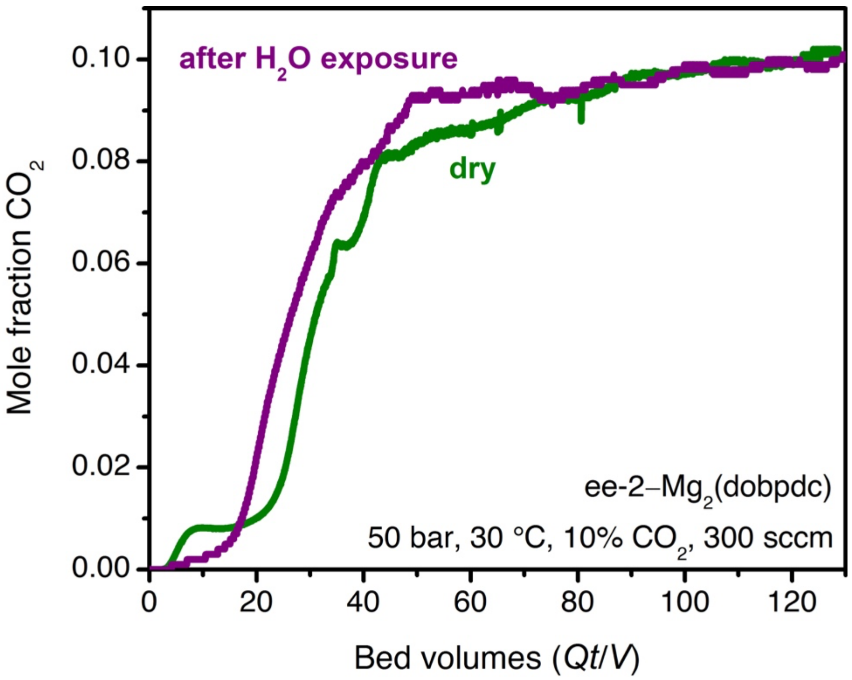

Figure S61. Dry breakthrough curve for ee-2–Mg_2(dobpdc) under 300 sccm of 10% CO_2 in CH_4 at 30 °C (green), and the same experiment performed after exposure of the material to H_2O (purple).

16. Characterization of ee-2–Mg_2(dobpdc) Following Extended Pressure Cycling

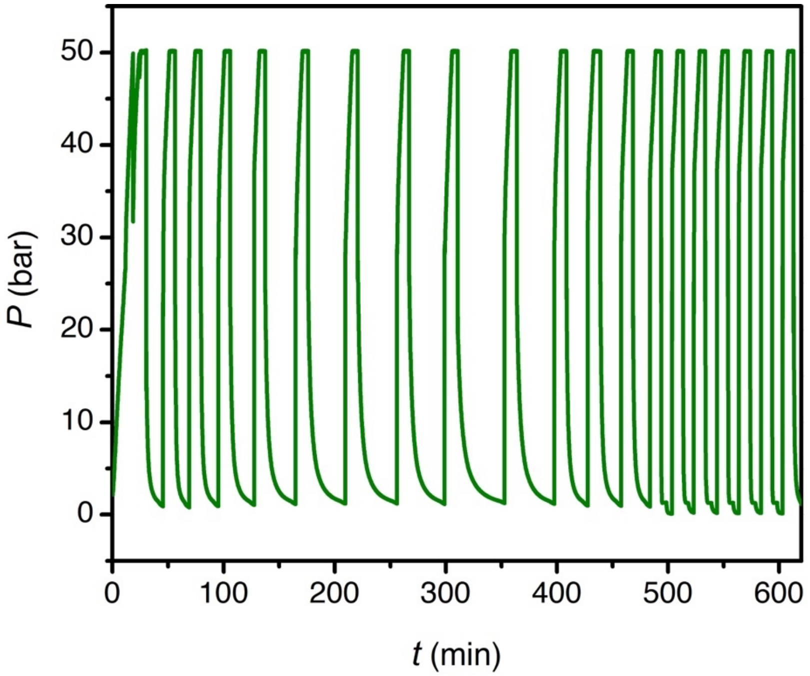

Figure S62. Pressure vs temperature data for one bed in the first 20 of 100 mechanical pressure cycles of ee-2–Mg_2(dobpdc) under 250 sccm of dry 10% CO_2 in CH_4 at 40 °C.

Table S11. Predicted and measured elemental analysis for ee-2–Mg_2(dobpdc) before and after extended pressure cycling. Materials were activated at 120 °C under vacuum for 2 h and stored in a N_2-filled glovebox prior to air-free elemental analysis. These results suggest contamination with co-fluidized glass wool packing, as confirmed with additional data below.

	Predicted for Mg_2(dobpdc)(ee-2)$_2$	**Measured, pre-cycling**	**Measured, post-cycling**
C	56.65	56.42	49.88
H	6.95	6.77	5.66
N	10.16	10.15	7.94

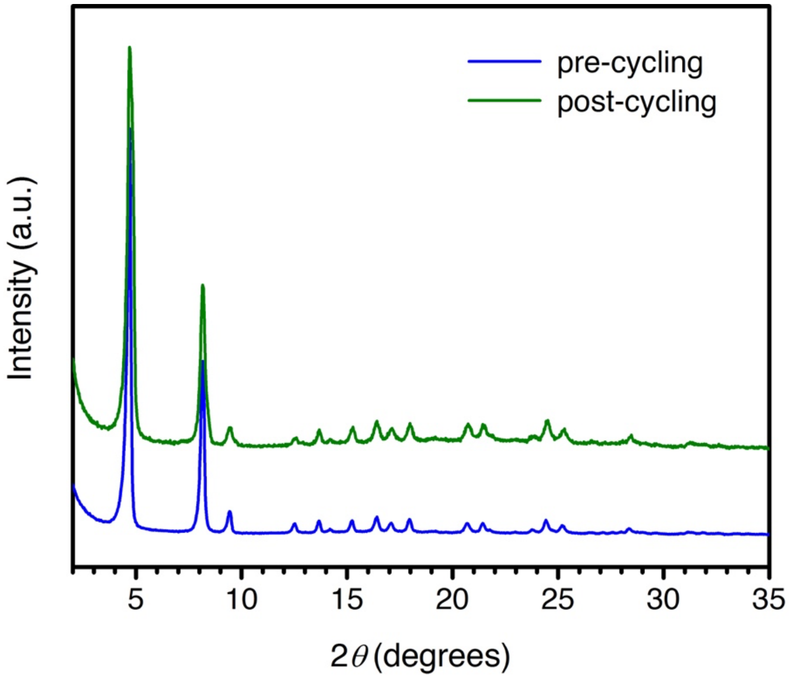

Figure S63. Laboratory powder X-ray diffraction patterns (λ = 1.5418 Å) for ee-2–Mg_2(dobpdc) before (blue) and after (green) extended pressure–vacuum cycling, demonstrating negligible changes in crystallinity.

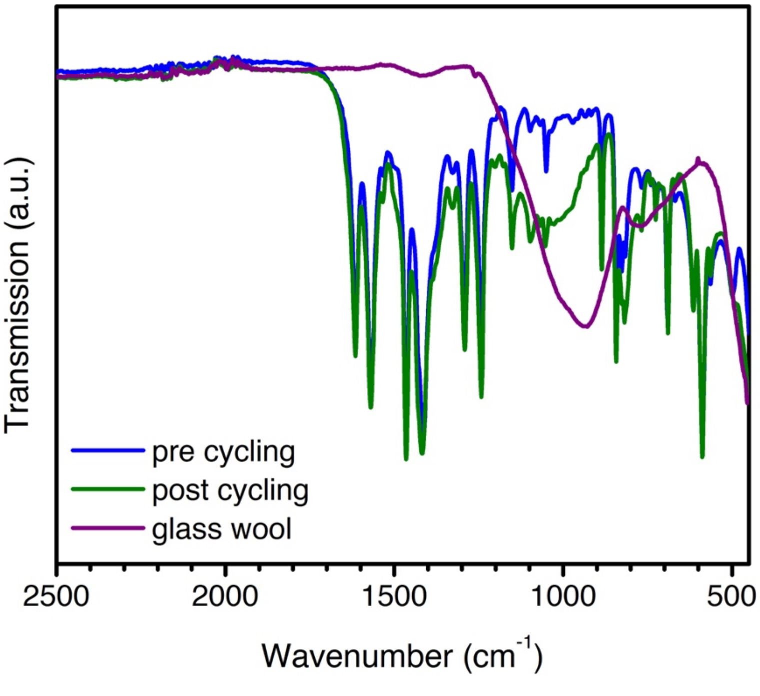

Figure S64. Infrared spectra of ee-2–Mg_2(dobpdc) before (blue) and after (green) extended pressure–vacuum cycling. A broad vibration was observed around 950 cm^{-1} and was assigned as glass wool packing (purple) that fluidized with the sample during cycling.

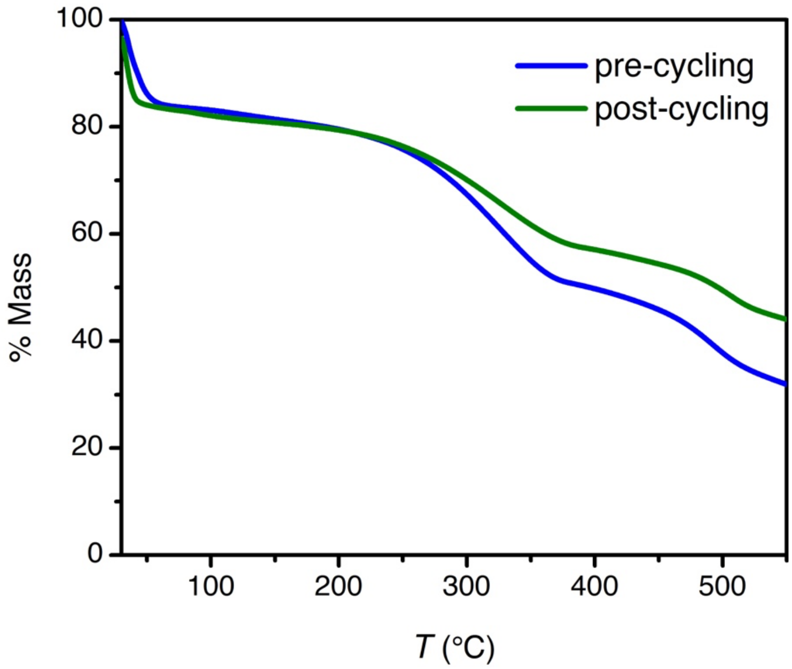

Figure S65. Thermogravimetric decomposition traces for ee-2–Mg_2(dobpdc) before (blue) and after (green) extended pressure–vacuum cycling. A temperature ramp rate of 1.5 °C/min was used. The higher baseline mass for the post-cycling sample at elevated temperatures is consistent with buildup of fluidized glass wool packing in the sample. To estimate the amount of co-fluidized glass wool, the apparent weight percent of diamine in the adsorbent calculated from the post-cycling decomposition curve (31 wt % between 150 and 420 °C) was compared to the weight percent of diamine in the adsorbent calculated from the pre-cycling decomposition curve (42 wt %). These results suggest glass wool contamination of approximately 26% by mass (100%*(1 − 0.31/0.42) = 26%), assuming no diamine loss during cycling. The assumption of negligible diamine loss was validated by collection of NMR spectra of the digested material before and after cycling. In both cases, full diamine loading was calculated from the ratio of the ligand and diamine peak integrals.

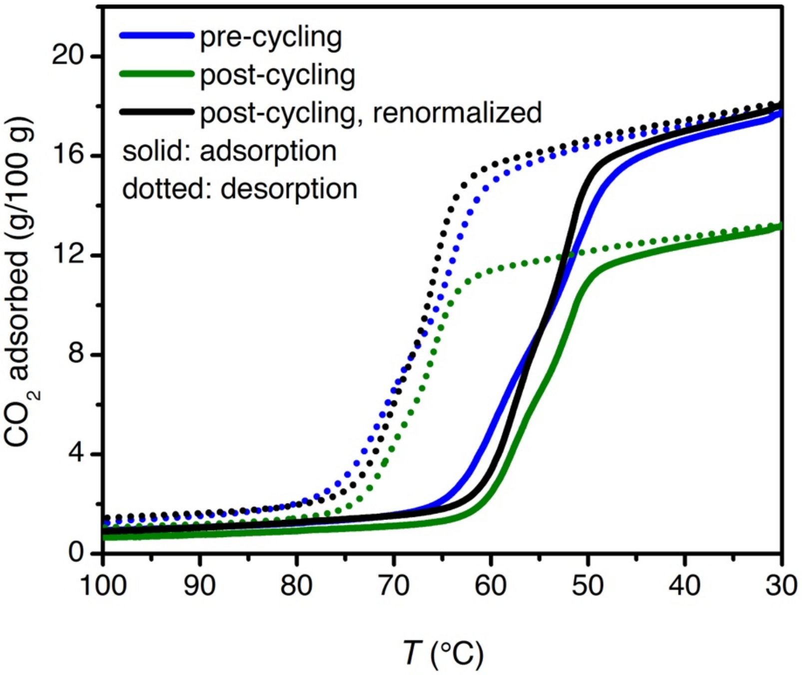

Figure S66. Dry, pure CO_2 adsorption isobars at atmospheric pressure for ee-2–Mg_2(dobpdc) before (blue) and after (green) extended pressure–vacuum cycling. Samples were activated at 120 °C under flowing N_2 for 30 min prior to isobar collection. A ramp rate of 1 °C/min was used. To account for the mass of co-fluidized glass wool contamination, the activated mass of adsorbent in the post-cycling isobar was renormalized using the estimated mass % of glass wool contamination determined from the TGA decomposition traces (Figure S65).

17. Synchrotron Powder X-ray Diffraction

High-resolution powder X-ray diffraction patterns of ee-2–Mg_2(dobpdc) and ee-2–Mg_2(dobpdc)–CO_2 were collected at beamline 17-BM at the Advance Photon Source of Argonne National Laboratory. An average wavelength of 0.45399 Å was used. Scattered intensity was recorded with a PerkinElmer a-Si Flat Panel detector. Prior to measurement, the sample was packed in a borosilicate glass capillary of 1.0 mm diameter under a N_2 atmosphere. The capillary was then attached to a custom-designed gas-dosing cell, which was then mounted onto the goniometer head and connected to a gas-dosing manifold for *in situ* diffraction measurements. The sample temperature was controlled by an Oxford Cryosystems Cryostream 800. The diffraction pattern of ee-2–Mg_2(dobpdc) was collected at 300 K under dynamic vacuum. The gas-dosing manifold was then used to dose the sample with 970 mbar of dry CO_2 at 300 K. The diffraction pattern of ee-2–Mg_2(dobpdc)–CO_2 was collected upon equilibration, as determined by stabilization of the diffraction pattern over several scans. Initial unit cell dimensions were determined by a standard peak search followed by indexing via single-value decomposition in TOPAS-Academic v4.1. Using TOPAS-Academic, precise unit cell dimensions were then determined by performing a structureless Pawley refinement.

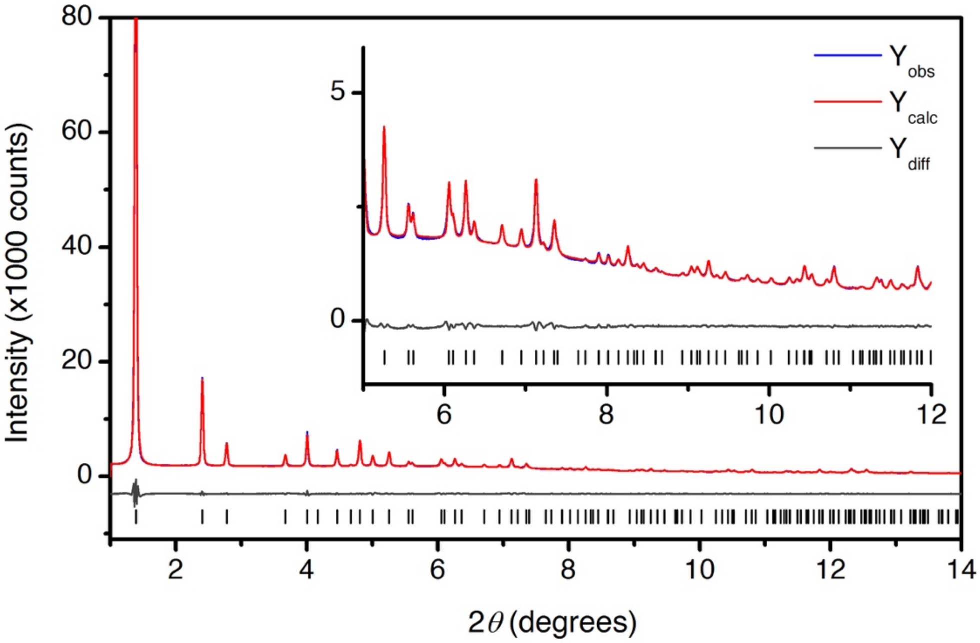

Figure S67. Pawley refinement of synchrotron powder X-ray diffraction data (λ = 0.45399 Å) for evacuated ee-2–Mg_2(dobpdc) at 300 K. Blue and red lines depict the observed and calculated diffraction patterns, respectively. The gray line depicts the difference between the observed and calculated patterns, and the black tick marks indicate the calculated Bragg peak positions. The inset shows the high-angle region at magnified scale. Figures-of-merit (as defined by TOPAS): R_{wp} = 2.13%, R_{exp} = 2.14%, R_p = 1.39%, GoF = 0.998.

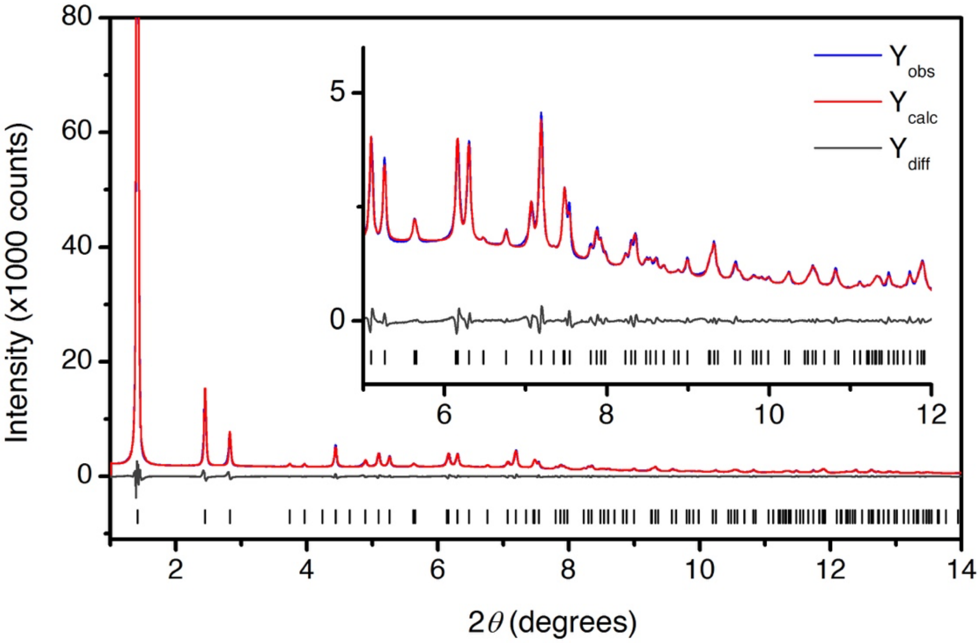

Figure S68. Pawley refinement of synchrotron powder X-ray diffraction data (λ = 0.45399 Å) for ee-2–Mg_2(dobpdc) dosed with 970 mbar of CO_2 at 300 K. Blue and red lines depict the observed and calculated diffraction patterns, respectively. The gray line depicts the difference between the observed and calculated patterns, and the black tick marks indicate the calculated Bragg peak positions. The inset shows the high-angle region at magnified scale. Figures-of-merit (as defined by TOPAS): R_{wp} = 3.37%, R_{exp} = 2.07%, R_p = 2.21%, GoF = 1.63.

Table S12. Crystallographic data for Pawley refinement of synchrotron powder X-ray diffraction data.

	ee-2–Mg_2(dobpdc), evacuated	ee-2–Mg_2(dobpdc), 970 mbar CO_2
Temperature (K)	300	300
Crystal System	Trigonal	Trigonal
Space Group	$P3_221$	$P3_221$
a, b, c (Å)	21.6248(1) 21.6248(1), 6.9188(3)	21.264(2) 21.264(2), 7.0289(5)
α, β, γ (°)	90, 90, 120	90, 90, 120
V (Å^3)	2801.9(3)	2752.3(4)
Radiation, λ (Å)	Synchrotron, 0.45399	Synchrotron, 0.45399
R_{wp}	2.13	3.37
R_{exp}	2.14	2.07
R_p	1.39	2.21
Goodness of Fit	0.998	1.63

18. Single-Crystal X-ray Diffraction

Single crystals of Zn_2(dobpdc) were prepared as reported previously.[6] The crystals were functionalized with the diamine ee-2 following a previously reported procedure.[1]

For CO_2 dosing, crystals of ee-2-Zn_2(dobpdc) were activated for 1 h at 100 °C under vacuum (<10 microbar) and then transferred to the analysis port of a Micromeritics ASAP 2420 gas sorption analyzer. The crystals were placed under 1100 mbar of CO_2 for 5 min at room temperature. The glass adsorption tube was then sealed under this CO_2 atmosphere, removed from the instrument, and stored over dry ice for 28 h. Immediately after removing the seal on the glass adsorption tube, the crystals were coated with Paratone oil, and a single crystal was rapidly mounted on a MiTeGen loop and frozen at a temperature of 100 K in a cryostream of N_2.

Single-crystal X-ray diffraction data were collected at Beamline 12.2.1 at the Advanced Light Source, Lawrence Berkeley National Laboratory using synchrotron radiation (λ = 0.7288 Å) and a Bruker AXS D8 diffractometer equipped with a Bruker PHOTON II CMOS detector. Structures were collected at 100 K using an Oxford Cryosystems Cryostream 700 Plus. Raw data were corrected for Lorentz and polarization effects using Bruker AXS SAINT software[15] and were corrected for absorption using SADABS.[16] The structures were solved using SHELXT[17] and refined using SHELXL[18] operated in the OLEX2[19] interface.

Thermal parameters were refined anisotropically for all non-hydrogen atoms. All hydrogen atoms were placed in ideal positions and refined using a riding model. The ammonium carbamate chains formed upon CO_2 adsorption (part -1 in the .cif) freely refined to an occupancy of 0.345(5). In addition, unreacted diamine was resolved in the structure (part -2 in the .cif) and freely refined to an occupancy of 0.451(8). These occupancies were fixed in the final refinement. Additionally, the occupancy of atom O4 (the bound oxygen atom of the carbamate) was fixed as (1 − the occupancy of the unreacted diamine) = 0.549 to account for water, solvent, or unreacted CO_2 at the open Zn(II) coordination sites not bound to carbamate groups or unreacted diamine. This decision was made on the basis of free refinement of the bound nitrogen and oxygen atoms, which gave occupancies of N3 = 0.41(5) (within error of the occupancy of unreacted diamine) and O4 = 0.55(5) (within error of 1 − the occupancy of unreacted diamine), respectively.

To model the disorder, the following distance and displacement parameter restraints were used:

SADI for 1,2 distances of C–C bonds in the ethyl groups of the diamine,

SADI for 1,2 distances of the C–N bonds of the tertiary amine in part -2, DFIX for the C–N bonds of the ammonium, and

RIGU and SIMU for the unreacted diamine (part -2)

Four instances of OMIT were used (OMIT 0 1 0, OMIT -1 1 1, OMIT 0 3 0, OMIT -4 4 2). These reflections were suspected to be affected by the beamstop.

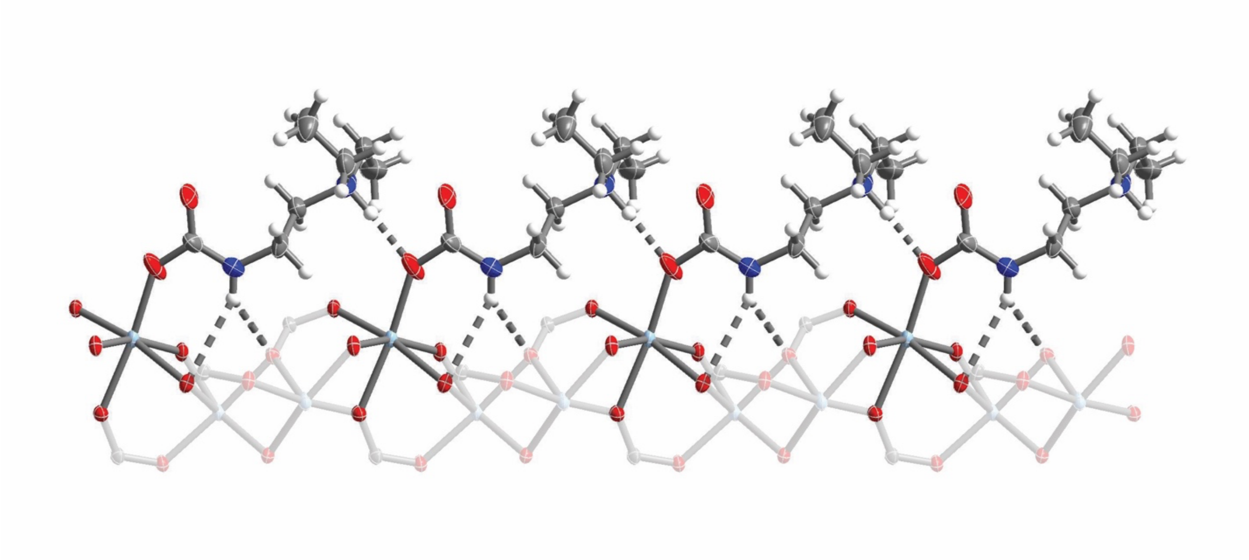

Figure S69. Thermal ellipsoid plot of the ammonium carbamate chains in Zn_2(dobpdc)(ee-2)$_{0.902}$(ee-2–CO_2)$_{0.690}$ at 100 K drawn at 50% probability level, as determined by single-crystal X-ray diffraction. Light blue, gray, blue, red, and white represent Zn, C, N, O, and H atoms, respectively.

Table S13. Crystallographic data for single-crystal X-ray diffraction.

	$Zn_2(dobpdc)(ee\text{-}2)_{0.902}(ee\text{-}2\text{–}CO_2)_{0.690}$
Formula	$C_{24.24}H_{31.47}N_{3.18}O_{7.38}Zn_2$
Temperature (K)	100(2)
Crystal System	Trigonal
Space Group	$P3_121$
a, b, c (Å)	21.5982(10), 21.5982(10), 6.9071(4)
α, β, γ (°)	90, 90, 120
V (Å^3)	2790.4(3)
Z	3
Radiation, λ (Å)	Synchrotron, 0.7288
2Θ Range for Data Collection (°)	3.868 to 59.814
Completeness to 2Θ	99.8% (2Θ = 51.860°)
Data / Restraints / Parameters	5009/ 95 / 274
Goodness of Fit on F^2	1.086
$R_1{}^a$, $wR_2{}^b$ (I>$2\sigma(I)$)	0.0335, 0.0877
$R_1{}^a$, $wR2^b$ (all data)	0.0395, 0.0906
Largest Diff. Peak and Hole (e Å^{-3})	0.379, –0.446

19. References

1 R. L. Siegelman, T. M. McDonald, M. I. Gonzalez, J. D. Martell, P. J. Milner, J. A. Mason, A. H. Berger, A. S. Bhown and J. R. Long, *J. Am. Chem. Soc.*, 2017, **139**, 10526–10538.

2 A. Boller, Y. Jin and B. Wunderlich, *J. Therm. Anal.*, 1994, **42**, 307–330.

3 *Gas Treating Chemicals, Vol. 1*, Union Carbide Chemicals Company, 1957.

4 P. J. Milner, R. L. Siegelman, A. C. Forse, M. I. Gonzalez, T. Runčevski, J. D. Martell, J. A. Reimer and J. R. Long, *J. Am. Chem. Soc.*, 2017, **139**, 13541–13553.

5 J.-H. Lee, R. L. Siegelman, L. Maserati, T. Rangel, B. A. Helms, J. R. Long and J. B. Neaton, *Chem. Sci.*, 2018, **9**, 5197–5206.

6 R. L. Siegelman, P. J. Milner, A. C. Forse, J.-H. Lee, K. A. Colwell, J. B. Neaton, J. A. Reimer, S. C. Weston and J. R. Long, *J. Am. Chem. Soc.*, 2019, **141**, 13171–13186.

7 F. G. Helfferich and P. W. Carr, *J. Chromatogr. A*, 1993, **629**, 97–122.

8 F. M. Golden, Ph.D. Thesis, University of California, Berkeley, 1973.

9 W. Zhang, Y. Shan and A. Seidel-Morgenstern, *J. Chromatogr. A*, 2006, **1107**, 216–225.

10 M. Mazzotti and A. Rajendran, *Annu. Rev. Chem. Biomol. Eng.*, 2013, **4**, 119–141.

11 M. Hefti, L. Joss, Z. Bjelobrk and M. Mazzotti, *Faraday Discuss.*, 2016, **192**, 153–179.

12 A. Sinha, L. A. Darunte, C. W. Jones, M. J. Realff and Y. Kawajiri, *Ind. Eng. Chem. Res.*, 2017, **56**, 750–764.

13 L. Darunte, T. Sen, C. Bhawanani, K. S. Walton, D. S. Sholl, M. J. Realff and C. W. Jones, *Ind. Eng. Chem. Res.*, 2019, **58**, 366–377.

14 L&C Science: PSA Bench-Top Testing System Series, http://www.landcscience.com/PSA-1000.html, (accessed April 26, 2019).

15 *SAINT, APEX2, and APEX3 Software for CCD Diffractometers*, Bruker Analytical X-ray Systems Inc., Madison, WI, USA, 2014.

16 G. M. Sheldrick, *SADABS*, University of Göttingen, Germany.

17 G. M. Sheldrick, *Acta Crystallogr. Sect. Found. Adv.*, 2015, **71**, 3–8.

18 G. M. Sheldrick, *Acta Crystallogr. Sect. C Struct. Chem.*, 2015, **71**, 3–8.

19 O. V. Dolomanov, L. J. Bourhis, R. J. Gildea, J. a. K. Howard and H. Puschmann, *J. Appl. Crystallogr.*, 2009, **42**, 339–341.